INTERNATIONAL JOURNAL FOR NUMERICAL METHODS IN FLUIDS, VOL. 25, 285–313 (1997)

SEMI-IMPLICIT FINITE VOLUME SHALLOW-WATER FLOW AND SOLUTE TRANSPORT SOLVER WITH k–ε TURBULENCE MODEL

PETER K. STANSBY*

Hydrodynamics Research Group, School of Engineering, University of Manchester, Manchester M13 9PL, U.K.

SUMMARY

A 3D semi-implicit finite volume scheme for shallow-water flow with the hydrostatic pressure assumption has been developed using the σ-co-ordinate system, incorporating a standard k–ε turbulence transport model and variable density solute transport with the Boussinesq approximation for the resulting horizontal pressure gradients. The mesh spacing in the vertical direction varies parabolically to give fine resolution near the bed and free surface to resolve high gradients of velocity, k and ε. In this study, wall functions are used at the bed (defined by the bed roughness) and wind stress at the surface is not considered. Surface elevation gradient terms and vertical diffusion terms are handled implicitly and horizontal diffusion and source terms explicitly, including the Boussinesq pressure gradient term due to the horizontal density gradient. The advection terms are handled in explicit (conservative) form using linear upwind interpolation giving second-order accuracy. A fully coupled solution for the flow field is obtained by substituting for velocity in the depth-integrated continuity equation and solving for surface elevation using a conjugate gradient equation solver. Evaluation of horizontal gradients in the σ-co-ordinate system requires high-order derivatives which can cause spurious flows and this is avoided by obtaining these gradients in real space. In this paper the method is applied to parallel oscillatory (tidal) flow in deep and shallow water and compared with field measurements. It is then applied to current flow about a conical island of small side slope where vortex shedding occurs and velocities are compared with data from the laboratory. Computed concentration distributions are also compared with dye visualization and an example of the influence of temperature on plume dispersion is presented. © 1997 by John Wiley & Sons, Ltd.

Int. J. Numer. Meth. Fluids, **25**: 285–313 (1997).

No. of Figures: 24. No. of Tables: 0. No. of References: 19.

KEY WORDS: shallow-water; solute; solver; turbulence; model

1. INTRODUCTION

Computational schemes for the simulation of the shallow-water equations in depth-averaged form have been widely used since the pioneering work of Leendertse.[1] Since then a wide variety of schemes have been produced encompassing much of what is generally available in computational fluid dynamics (CFD): finite difference, finite volume and finite element methods for spatial discretization; explicit and implicit time stepping; alternating direction implicit (ADI), multigrid and

* Correspondence to: P. K. Stansby, Division of Civil Engineering, The Manchester School of Engineering, Simon Building, Oxford Road, Manchester M13 9PL, U.K.

Contract grant sponsor: EPSRC; Contract grant number: GR/K95666

CCC 0271–2091/97/030285–29 $17.50 *Received October 1996*

conjugate gradient equation solving; non-conservative and conservative equation choice. Turbulence modelling has been limited to the eddy viscosity approach, with either a simple empirical formula (constant or proportional to friction velocity and depth) or k–l transport modelling, where k is the turbulent kinetic energy and l is its length scale, given by a simple algebraic formula. Rectangular and boundary-fitted meshes have been applied, although in this context the latter does not imply dynamic meshing, fitting the moving wet/dry boundaries; rather a fixed mesh is set up which covers the maximum extent of wetted area. This is intended to improve computational efficiency and reduce storage requirements.

In this paper we are concerned with the 3D shallow-water equations and solute transport which have become a practical computing possibility over the last few years with increasing computing power and storage. Hydrostatic pressure is assumed with the implication that horizontal pressure gradients are independent of depth below the surface. Thus separation in a vertical plane cannot be reproduced generally which can be a significant limitation with recirculating flows even for gently sloping bathymetries,[2] but this matter will not be addressed here. Various multiple-level models have been developed in real (Cartesian) space where friction is specified at a layer interface and simple formulae for eddy viscosity are used, e.g. those of Kawahara *et al.*[3] and Lynch and Werner.[4] A similar approach, only using a vertically coupled finite difference scheme, has been adopted by Lin and Falconer[5] using the ADI approach and Casulli and Cheng[6] using Lagrangian advection. Other schemes have been formulated with equations in σ-co-ordinate form in the vertical (fitted to the bed and water surface) following the practice in atmospheric aerodynamics (after Phillips[7]). The ADI scheme has been applied in 3D by Uittenbogaard *et al.*[8] and the Casulli and Cheng scheme has been set up in σ-co-ordinates by Stansby and Lloyd.[9] Both the latter are semi-implicit and fully coupled in orthogonal horizontal directions using conjugate gradient equation solving. Eddy viscosity turbulence modelling of mixing length form has been applied in the references above (apart from Reference 8 which has various options including k–l modelling). Use of mixing length and k–l models has been assessed by Davies and Jones[10] for equations in linearized form appropriate for some tidal computations. Use of a more complete approach with transport equations for k and ε, the turbulence energy dissipation rate, has yet to be applied in this context to the author's knowledge. It should also be pointed out that in other areas of engineering, notably aeronautical, more advanced anisotropic turbulence modelling is being employed: non-linear k–ε modelling (e.g. Reference 11) and full Reynolds stress transport modelling, albeit at substantial computational expense for the latter. However, these flows do not have the complication of a moving free surface with wetting and drying of cells. The level of turbulence modelling required or desirable for a particular application is a rather open question, depending for example on whether broad flow features are required or detailed long-term concentration distributions. However, it can be said that a simple mixing length model produced good general flow predictions including recirculations in steady ambient flows around islands,[2,9] while for oscillatory ambient flows more complex turbulence structures occur which are bound to be significant for solute dispersion and a higher level of turbulence model is desirable. The k–ε model has been suggested as the minimum level for the related problem of oscillatory boundary layer flow over a flat bed due to surface waves.[12] In this paper the aim is to incorporate the standard k–ε turbulence model with wall functions (e.g. Reference 13) into a 3D shallow-water scheme in the knowledge that extending to non-linear k–ε modelling would be straightforward. Rough turbulent boundary layers are assumed throughout since this usually occurs in practice. The numerical approach derives from the experience of Stansby and Lloyd.[9] All vertical diffusion terms are handled implicitly and horizontal diffusion and source terms, including the Boussinesq pressure term due to variable density, explicitly. First-order time stepping is maintained since it will be shown that a much smaller time step is needed for stability with k–ε modelling than with the mixing length turbulence model. The equations are solved in σ-co-ordinate form since we believe it is essential to represent

accurately regions close to the bed and surface where sharp gradients occur and mesh compression is now applied. The finite volume method is applied with the equations in conservative form. Inaccuracies do occur in σ-co-ordinates through the evaluation of horizontal gradient terms and to avoid this we compute these in real space following Stelling and van Kester.[14] The advection terms are handled explicitly (in conservative form) with upwind differencing. The velocities thus obtained from the momentum equations are substituted into the depth-averaged continuity equation and the resulting equations for surface elevation are solved by a conjugate gradient scheme. All other flow and scalar quantities may then be obtained to complete a time step.

Finally the scheme is set up with a rectangular horizontal mesh. It is found that most of the computational effort goes into setting up the elements of the matrix equation for wet cells prior to the solution for surface elevation and then subsequent to the solution in obtaining required quantities. The time required for solution itself by the conjugate gradient method is a negligible proportion of a time step and thus there would be little or no benefit in a horizontally boundary fitted mesh with 3D computations, at least for many configurations.

The overall aim of the paper is thus to establish a robust and efficient scheme with k–ε turbulence modelling for the 3D equations in conservative form in σ-co-ordinates and to demonstrate prediction capability and computing requirements. To check the method, some 1D vertical computations are undertaken for uniform oscillatory flow: the turbulent bed boundary layer due to linear surface waves to compare with the results of Justesen[12] and tidal flows in the Jade and Elbe estuaries to compare with Baumert and Radach[15] for which some full-scale flow and turbulence measurements are available. To test the stability of the 3D scheme with wetting and drying, the island flow of Stansby and Lloyd[9] is recomputed and compared with experimental data. Solute is added to the computation to compare qualitatively with experimental dye visualizations[2] for cases with rather different vortex shedding. Examples of the influence of non-ambient plume temperature on its dispersion around an island are also presented.

2. MATHEMATICAL FORMULATION

Definitions of water surface elevation η, water depth h and bed elevation z_0 are shown in Figure 1.

Starting from the Navier–Stokes and continuity equations and taking mean quantities in an averaging time δt which is small in relation to the time scales of the large-scale slowly varying structures of a flow, we obtain the Reynolds equation system. We then accept the Boussinesq assumption relating the turbulent stresses introduced by the averaging processes to the mean velocity gradients. The resulting equation set may thus be defined as the continuity equation

$$\frac{\partial u}{\partial x}+\frac{\partial v}{\partial y}+\frac{\partial w}{\partial z}=0, \tag{1}$$

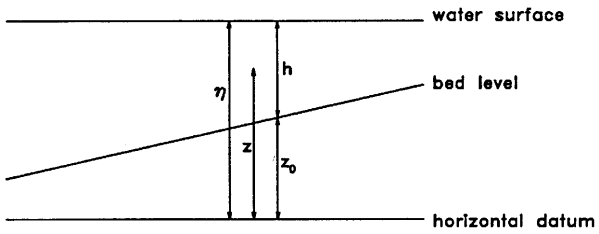

Figure 1. Definition sketch

the momentum equations for the orthogonal horizontal directions x and y with the total derivative also expressed in conservative form,

$$\frac{\mathrm{D}u}{\mathrm{D}t} = \frac{\partial u}{\partial t} + \frac{\partial (u^2)}{\partial x} + \frac{\partial (uv)}{\partial y} + \frac{\partial (uw)}{\partial z} = -\frac{1}{\rho}\frac{\partial p}{\partial x} + \frac{\partial}{\partial x}\left(\nu_{\mathrm{E}}\frac{\partial u}{\partial x}\right) + \frac{\partial}{\partial y}\left(\nu_{\mathrm{E}}\frac{\partial u}{\partial y}\right) + \frac{\partial}{\partial z}\left(\nu_{\mathrm{E}}\frac{\partial u}{\partial z}\right), \tag{2}$$

$$\frac{\mathrm{D}v}{\mathrm{D}t} = \frac{\partial v}{\partial t} + \frac{\partial (uv)}{\partial x} + \frac{\partial (v^2)}{\partial y} + \frac{\partial (vw)}{\partial z} = -\frac{1}{\rho}\frac{\partial p}{\partial y} + \frac{\partial}{\partial x}\left(\nu_{\mathrm{E}}\frac{\partial v}{\partial x}\right) + \frac{\partial}{\partial y}\left(\nu_{\mathrm{E}}\frac{\partial v}{\partial y}\right) + \frac{\partial}{\partial z}\left(\nu_{\mathrm{E}}\frac{\partial v}{\partial z}\right), \tag{3}$$

and in the vertical direction z the pressure p is assumed to be hydrostatic,

$$\frac{1}{\rho}\frac{\partial p}{\partial z} = -g, \tag{4}$$

where u, v and w are velocities in the directions x, y and z respectively and ν_{E} is the turbulent eddy viscosity (kinematic) defined by the turbulence energy k and dissipation rate ε such that

$$\nu_{\mathrm{E}} = \nu + c_\mu \frac{k^2}{\varepsilon}. \tag{5}$$

Here k and ε are defined by the standard transport equations,[13] without accounting for stratification effects, again with the total derivative in conservative form:

$$\frac{\mathrm{D}k}{\mathrm{D}t} = \frac{\partial k}{\partial t} + \frac{\partial (uk)}{\partial x} + \frac{\partial (vk)}{\partial y} + \frac{\partial (wk)}{\partial z} = \frac{\partial}{\partial x}\left(\frac{\nu_{\mathrm{E}}}{\sigma_k}\frac{\partial k}{\partial x}\right) + \frac{\partial}{\partial y}\left(\frac{\nu_{\mathrm{E}}}{\sigma_k}\frac{\partial k}{\partial y}\right) + \frac{\partial}{\partial z}\left(\frac{\nu_{\mathrm{E}}}{\sigma_k}\frac{\partial k}{\partial z}\right) + P - \varepsilon, \tag{6}$$

$$\frac{\mathrm{D}\varepsilon}{\mathrm{D}t} = \frac{\partial \varepsilon}{\partial t} + \frac{\partial (u\varepsilon)}{\partial x} + \frac{\partial (v\varepsilon)}{\partial y} + \frac{\partial (w\varepsilon)}{\partial z} = \frac{\partial}{\partial x}\left(\frac{\nu_{\mathrm{E}}}{\sigma_\varepsilon}\frac{\partial \varepsilon}{\partial x}\right) + \frac{\partial}{\partial y}\left(\frac{\nu_{\mathrm{E}}}{\sigma_\varepsilon}\frac{\partial \varepsilon}{\partial y}\right) + \frac{\partial}{\partial z}\left(\frac{\nu_{\mathrm{E}}}{\sigma_\varepsilon}\frac{\partial \varepsilon}{\partial z}\right) + c_{1\varepsilon}\frac{\varepsilon}{k}P - c_{2\varepsilon}\frac{\varepsilon^2}{k}. \tag{7}$$

The turbulence production term P is given compactly in tensor notation as

$$P = \nu_{\mathrm{E}}\left(\frac{\partial u_i}{\partial x_j} + \frac{\partial u_j}{\partial x_i}\right)\frac{\partial u_i}{\partial x_j}, \tag{8}$$

where $i = 1, 2, 3$ correspond to the co-ordinates x, y and z respectively. Standard values of the turbulence constants are used: $c_\mu = 0{\cdot}09$, $c_{1\varepsilon} = 1{\cdot}44$, $c_{2\varepsilon} = 1{\cdot}92$, $\sigma_k = 1{\cdot}0$ and $\sigma_\varepsilon = 1{\cdot}3$.

The diffusion–advection equation for the transport of solute concentration (or temperature) c is given by

$$\frac{\mathrm{D}c}{\mathrm{D}t} = \frac{\partial c}{\partial t} + \frac{\partial (uc)}{\partial x} + \frac{\partial (vc)}{\partial y} + \frac{\partial (wc)}{\partial z} = \frac{\partial}{\partial x}\left(\frac{\nu_{\mathrm{E}}}{\sigma_c}\frac{\partial c}{\partial x}\right) + \frac{\partial}{\partial y}\left(\frac{\nu_{\mathrm{E}}}{\sigma_c}\frac{\partial c}{\partial y}\right) + \frac{\partial}{\partial z}\left(\frac{\nu_{\mathrm{E}}}{\sigma_c}\frac{\partial c}{\partial z}\right), \tag{9}$$

where σ_c is the turbulent Schmidt number.

To determine the horizontal pressure gradient terms in (2) and (3), since $\rho = \rho(x, y, z, t)$ and solute is not neutrally buoyant in general, $\rho = \rho(c(x, y, z, t))$. Integrating (4) gives

$$p(x, y, z, t) = \int_{z'=z}^{\eta(x,y,t)} g\rho(x, y, z', t)\mathrm{d}z'. \tag{10}$$

Applying the Leibniz rule and dropping the independent variables for compactness gives

$$\frac{\partial p}{\partial x} = \frac{\partial}{\partial x}\int_{z'=z}^{\eta} g\rho \, \mathrm{d}z' = \int_{z'=z}^{\eta} g\frac{\partial \rho}{\partial x}\mathrm{d}z' + g\rho_\eta \frac{\partial \eta}{\partial x}, \tag{11}$$

where ρ_η is the density at the surface and there is a corresponding expression for $\partial p/\partial y$. For small density variations the Boussinesq approximation is valid:

$$\frac{1}{\rho}\frac{\partial p}{\partial x} = \frac{1}{\rho_0}\frac{\partial p}{\partial x} = g\frac{\rho_\eta}{\rho_0}\frac{\partial \eta}{\partial x} + \frac{g}{\rho_0}\int_{z'=z}^{\eta}\frac{\partial \rho}{\partial x}\mathrm{d}z', \tag{12}$$

where ρ_0 is a reference density (usually that of fresh water). The first term on the right-hand side will be treated implicitly and the second term, which is by definition small, explicitly.

The equation set is completed by integrating the continuity equation over depth and applying the kinematic free surface condition and the Leibniz rule again to give the 'depth-integrated' continuity equation

$$\frac{\partial \eta}{\partial t} + \frac{\partial}{\partial x}\int_{z=z_0}^{\eta} u\mathrm{d}z + \frac{\partial}{\partial y}\int_{z=z_0}^{\eta} v\,\mathrm{d}z = 0. \tag{13}$$

Standard wall functions are used as boundary conditions at the bed.[13] The logarithmic law of the wall is used to relate the velocity just above the bed to the bed friction velocity $u_* = \sqrt{(\tau_0/\rho)}$:

$$\frac{u_m}{u_*} = \frac{1}{\kappa}\ln\left(\frac{33(z-z_0)}{k_s}\right), \tag{14}$$

where τ_0 is the bed shear stress, $u_m = \sqrt{(u^2+v^2)}$ at a distance $z - z_0$ above the bed, κ is von Karman's constant, taken to be 0·43, and k_s is the roughness height. (We are here concerned only with rough turbulent boundary layers.) This wall region is valid for $30 < z^+ < 100$, where $z^+ = (z-z_0)u_*/\nu$. In the spatial discretization the first vertical mesh point should thus lie within this region, which is straightforward to arrange in mainly steady flows but is more problematic in oscillatory flows and is discussed later. The shear stress within the wall region may be assumed constant (for a given horizontal location) and for a given vertical position z_1 we have

$$u_* = \frac{u_{m1}}{(1/\kappa)\ln[33(z_1-z_0)/k_s]}. \tag{15}$$

The shear stress components in the directions x and y, τ_{0x} and τ_{0y} are resolved as

$$\frac{\tau_{0x}}{\rho} = \nu_E\frac{\partial u}{\partial z} = \gamma u_1, \qquad \frac{\tau_{0y}}{\rho} = \nu_E\frac{\partial v}{\partial z} = \gamma v_1, \tag{16}$$

where u_1 and v_1 are the velocities at z_1 and

$$\gamma = \frac{u_{m1}}{\{(1/\kappa)\ln[33(z_1-z_0)/k_s]\}^2}. \tag{17}$$

In the wall region the Reynolds stresses are assumed constant and turbulence production equals dissipation, giving

$$k = \frac{u_*^2}{\sqrt{c_\mu}}, \tag{18}$$

$$\varepsilon = \frac{u_*^3}{\kappa(z-z_0)}. \tag{19}$$

At the water surface, without wind stress, there is zero stress, implying $\partial u/\partial z = \partial v/\partial z = 0$. For k and ε we impose[13]

$$\frac{\partial k}{\partial z} = 0, \qquad \varepsilon = \frac{(k_{\text{surface}}\sqrt{c_\mu})^{3/2}}{0{\cdot}07\kappa h}. \tag{20}$$

There is also zero solute flux across the bed and water surface, implying $\partial c/\partial z = 0$. For the accurate implementation of these boundary conditions the numerical mesh is made to fit the bed and water surface by replacing the z-co-ordinate with a σ-co-ordinate defined by

$$\sigma = \frac{z - \eta}{h}. \tag{21}$$

In this frame $u_\sigma = u$, $v_\sigma = v$, $w_\sigma = \mathrm{D}\sigma/\mathrm{D}t$, $k_\sigma = k$, $\varepsilon_\sigma = \varepsilon$ and $c_\sigma = c$; also we use $\omega = hw_\sigma$ which is related to w through

$$\omega = w - u\left(\sigma\frac{\partial h}{\partial x} + \frac{\partial \eta}{\partial x}\right) - v\left(\sigma\frac{\partial h}{\partial y} + \frac{\partial \eta}{\partial y}\right) - \left(\sigma\frac{\partial h}{\partial t} + \frac{\partial \eta}{\partial t}\right). \tag{22}$$

The continuity equation becomes (dropping the suffix σ)

$$\frac{\partial \eta}{\partial t} + \frac{\partial (hu)}{\partial x} + \frac{\partial (hv)}{\partial y} + \frac{\partial \omega}{\partial \sigma} = 0 \tag{23}$$

and the total derivatives for u and v in the momentum equations and the scalar quantities k, ε and c have the same form. For example, for u (again dropping the suffix σ),

$$h\frac{\mathrm{D}u}{\mathrm{D}t} = \frac{\partial (hu)}{\partial t} + \frac{\partial (hu^2)}{\partial x} + \frac{\partial (huv)}{\partial y} + \frac{\partial (u\omega)}{\partial \sigma}. \tag{24}$$

The horizontal diffusion and pressure gradient terms involve additional derivative terms in a σ-co-ordinate system which can cause significant errors near steep bed slopes. For example, for p,

$$\frac{\partial p}{\partial x} = \frac{\partial p_\sigma}{\partial x_\sigma} + \frac{\partial \sigma}{\partial x}\frac{\partial p_\sigma}{\partial \sigma} = \frac{\partial p_\sigma}{\partial x_\sigma} - \frac{1}{h}\left(\frac{\partial \eta}{\partial x} + \sigma\frac{\partial h}{\partial x}\right)\frac{\partial p_\sigma}{\partial \sigma}. \tag{25}$$

We can thus have the sum of two significantly large terms of opposite sign with truncation errors causing a relatively large error in gradient. A numerical requirement to avoid significant spurious flow has been suggested such that

$$\left|\frac{\sigma}{h}\frac{\partial h}{\partial x}\right| < \frac{\delta\sigma}{\delta x}, \tag{26}$$

where δx and $\delta\sigma$ are mesh spacings.[16] In this scheme the problem is particularly significant since the mesh is compressed near the bed with a very small $\delta\sigma$-value. This is avoided by evaluating these terms in physical (x, y, z) space in a finite volume scheme.[14] The advective terms on the other hand are very conveniently obtained in σ-co-ordinates by the finite volume method since the physical space maps onto a cuboid in σ-space and there are no derivative terms to be evaluated.

In the numerical scheme we compress the σ-mesh near the bed and surface symmetrically about mid-depth to give greater definition using the parabolic transformation

$$\frac{\mathrm{d}\sigma_{\mathrm{mesh}}}{\mathrm{d}\sigma'_{\mathrm{mesh}}} = b(\sigma_{\mathrm{mesh}} + a)(1 - \sigma_{\mathrm{mesh}} + a), \tag{27}$$

where $0 \leqslant \sigma_{\text{mesh}} \leqslant 1$ defines the σ-mesh and $0 \leqslant \sigma'_{\text{mesh}} \leqslant 1$ is a uniformly spaced mesh. (Note that $\sigma = \sigma_{\text{mesh}} - 1$.) Here a and b are algebraically related constants ($a \ll 1$) which determine the degree of compression together with the number of vertical grid points, where

$$\begin{aligned} b &= \frac{2}{1+2a}\ln\left(1+\frac{1}{a}\right), \\ \sigma'_{\text{mesh}} &= \frac{1}{b(1+2a)}\ln\left(\frac{\sigma_{\text{mesh}}+a}{a}\frac{1+a}{1-\sigma_{\text{mesh}}+a}\right). \end{aligned} \tag{28}$$

At the bed (and surface) we thus have

$$\delta\sigma = \frac{\delta z}{h} \approx -\frac{2a\ln(a)}{K},$$

where K is the number of vertical cells.

3. NUMERICAL DISCRETIZATION

We use the conventional staggered mesh system shown in Figure 2 for the momentum equations to avoid checkerboard oscillations with cells numbered centrally i, j, k, where $i = 1, \ldots, I, j = 1, \ldots, J$ and $k = 1, \ldots, K$, with $k = 1$ for the bed cell and $k = K$ for the surface cell. The horizontal cell sizes are δx and δy. At this stage we consider the implicit terms with the explicit terms lumped together in the operator F which will be defined later. Note that for the pressure gradient terms of (12) the surface elevation term is treated implicitly and the small Boussinesq, density gradient term explicitly. Although we use the finite volume approach, it is convenient to make u and v the subject of the equations for later substitution. The momentum equations take the discretized form

$$\begin{aligned} u^{n+1}_{i+1/2,\,j,k} &= Fu^n_{i+1/2,\,j,k} - g\frac{\rho_{\eta_{i+1/2,\,j}}}{\rho_0}\frac{\delta t}{\delta x}(\eta^{n+1}_{i+1,\,j} - \eta^{n+1}_{i,\,j}) \\ &+ \delta t\frac{v^n_{i+1/2,\,j,k+1/2}\left(\dfrac{\partial\sigma'}{\partial\sigma}\right)_{k+1/2}(u^{n+1}_{i+1/2,\,j,k+1} - u^{n+1}_{i+1/2,\,j,k}) - v^n_{i+1/2,\,j,k-1/2}\left(\dfrac{\partial\sigma'}{\partial\sigma}\right)_{k-1/2}(u^{n+1}_{i+1/2,\,j,k} - u^{n+1}_{i+1/2,\,j,k-1})}{\delta\sigma'(h^n_{i+1/2,\,j})^2(\sigma_{k+1/2} - \sigma_{k-1/2})}, \end{aligned} \tag{29}$$

$$\begin{aligned} v^{n+1}_{i,\,j+1/2,k} &= Fv^n_{i,\,j+1/2,k} - g\frac{\rho_{\eta_{i,\,j+1/2}}}{\rho_0}\frac{\delta t}{\delta y}(\eta^{n+1}_{i,\,j+1} - \eta^{n+1}_{i,\,j}) \\ &+ \delta t\frac{v^n_{i,\,j+1/2,k+1/2}\left(\dfrac{\partial\sigma'}{\partial\sigma}\right)_{k+1/2}(v^{n+1}_{i,\,j+1/2,k+1} - v^{n+1}_{i,\,j+1/2,k}) - v^n_{i,\,j+1/2,k-1/2}\left(\dfrac{\partial\sigma'}{\partial\sigma}\right)_{k-1/2}(v^{n+1}_{i,\,j+1/2,k} - v^{n+1}_{i,\,j+1/2,k-1})}{\delta\sigma'(h^n_{i,\,j+1/2})^2(\sigma_{k+1/2} - \sigma_{k-1/2})}, \end{aligned} \tag{30}$$

where n denotes the time level, δt is the time step, $\delta\sigma' = 1/K$ and the subscript E has been omitted from v_{E} to avoid congestion. In compact matrix–vector form,

$$A^n_{i+1/2,\,j}U^{n+1}_{i+1/2,\,j} = G^n_{i+1/2,\,j} - g\frac{\rho_{\eta_{i+1/2,\,j}}}{\rho_0}\frac{\delta t}{\delta x}(\eta^{n+1}_{i+1,\,j} - \eta^{n+1}_{i,\,j})h^n_{i+1/2,\,j}\Delta\sigma, \tag{31}$$

$$A^n_{i,\,j+1/2}V^{n+1}_{i,\,j+1/2} = G^n_{i,\,j+1/2} - g\frac{\rho_{\eta_{i,\,j+1/2}}}{\rho_0}\frac{\delta t}{\delta y}(\eta^{n+1}_{i,\,j+1} - \eta^{n+1}_{i,\,j})h^n_{i,\,j+1/2}\Delta\sigma, \tag{32}$$

where

$$U^n_{i+1/2,\,j} = [u^n_{i+1/2,\,j,1}, \ldots, u^n_{i+1/2,\,j,K}]^{\mathrm{T}}, \qquad V^n_{i,\,j+1/2} = [v^n_{i,\,j+1/2,1}, \ldots, v^n_{i,\,j+1/2,K}]^{\mathrm{T}},$$

$$G^n_{i+1/2,\,j} = h^n_{i+1/2,\,j}\Delta\sigma^{\mathrm{T}}[Fu^n_{i+1/2,\,j,1}, \ldots, Fu^n_{i+1/2,\,j,K}]^{\mathrm{T}}, \tag{33}$$

$$G^n_{i,\,j+1/2} = h^n_{i,\,j+1/2}\Delta\sigma^{\mathrm{T}}[Fv^n_{i,\,j+1/2,1}, \ldots, Fv^n_{i,\,j+1/2,K}]^{\mathrm{T}},$$

$$\Delta\sigma = [\delta\sigma_1, \ldots, \delta\sigma_K]^{\mathrm{T}}, \tag{34}$$

with $\delta\sigma_k = \sigma_{k+1/2} - \sigma_{k-1/2}$. Note $\sigma_{1/2}$ corresponds to the bed and $\sigma_{K+1/2}$ to the surface in this notation. The tridiagonal matrix A has different forms for the directions x and y although omitting the subcripts $(i+\frac{1}{2}, j)$ and $(i,\ j+\frac{1}{2})$ the elements a_{lk} are defined in both cases by: for $k=1$,

$$a_{11} = h\delta\sigma_1 + \gamma\delta t + \delta t\frac{v_{3/2}\left(\dfrac{\mathrm{d}\sigma'}{\mathrm{d}\sigma}\right)_{3/2}}{h\delta\sigma'},$$

$$a_{12} = -\delta t\frac{v_{3/2}\left(\dfrac{\mathrm{d}\sigma'}{\mathrm{d}\sigma}\right)_{3/2}}{h\delta\sigma'}; \tag{35a}$$

for $k = 2, \ldots, K-1$,

$$a_{k,k-1} = -\delta t\frac{v_{k-1/2}\left(\dfrac{\mathrm{d}\sigma'}{\mathrm{d}\sigma}\right)_{k-1/2}}{h\delta\sigma'},$$

$$a_{k,k} = h\delta\sigma_k + \delta t\frac{v_{k+1/2}\left(\dfrac{\mathrm{d}\sigma'}{\mathrm{d}\sigma}\right)_{k+1/2}}{h\delta\sigma'} + \delta t\frac{v_{k-1/2}\left(\dfrac{\mathrm{d}\sigma'}{\mathrm{d}\sigma}\right)_{k-1/2}}{h\delta\sigma'}, \tag{35b}$$

$$a_{k,k+1} = -\delta t\frac{v_{k+1/2}\left(\dfrac{\mathrm{d}\sigma'}{\mathrm{d}\sigma}\right)_{k+1/2}}{h\delta\sigma'},$$

for $k=K$,

$$a_{K,K-1} = -\delta t\frac{v_{K-1/2}\left(\dfrac{\mathrm{d}\sigma'}{\mathrm{d}\sigma}\right)_{K-1/2}}{h\delta\sigma'},$$

$$a_{K,K} = h\delta\sigma_K + \delta t\frac{v_{K-1/2}\left(\dfrac{\mathrm{d}\sigma'}{\mathrm{d}\sigma}\right)_{K-1/2}}{h\delta\sigma'}. \tag{35c}$$

Substituting into the depth-integrated continuity equation gives

$$\eta^{n+1}_{i,\,j} = \eta^n_{i,\,j} - \frac{\delta t}{\delta x}(h^n_{i+1/2,\,j}\Delta\sigma^{\mathrm{T}}U^{n+1}_{i+1/2,\,j} - h^n_{i-1/2,\,j}\Delta\sigma^{\mathrm{T}}U^{n+1}_{i-1/2,\,j})$$

$$-\frac{\delta t}{\delta y}(h^n_{i,\,j+1/2}\Delta\sigma^{\mathrm{T}}V^{n+1}_{i,\,j+1/2} - h^n_{i,\,j-1/2}\Delta\sigma^{\mathrm{T}}V^{n+1}_{i,\,j-1/2}). \tag{36}$$

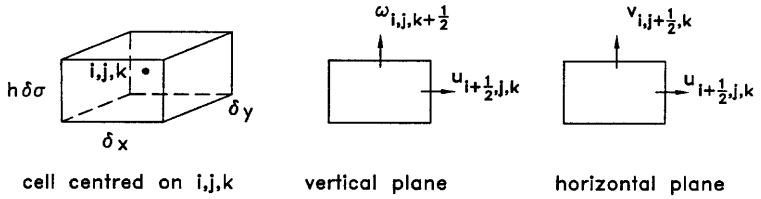

Figure 2. Sketch showing staggered mesh system

Substituting for U and V gives

$$\begin{aligned}
\eta_{i,j}^{n+1} - g\frac{\rho_{\eta_{i+1/2,j}}}{\rho_0}\frac{\delta t^2}{\delta x^2}&[(h_{i+1/2,j}^{n})^2\Delta\sigma^{\mathrm{T}}A_{i+1/2,j}^{-1}\Delta\sigma(\eta_{i+1,j}^{n+1}-\eta_{i,j}^{n+1})\\
&-(h_{i-1/2,j}^{n})^2\Delta\sigma^{\mathrm{T}}A_{i-1/2,j}^{-1}\Delta\sigma(\eta_{i,j}^{n+1}-\eta_{i-1,j}^{n+1})]\\
&-g\frac{\rho_{\eta_{i,j+1/2}}}{\rho_0}\frac{\delta t^2}{\delta y^2}[(h_{i,j+1/2}^{n})^2\Delta\sigma^{\mathrm{T}}A_{i,j+1/2}^{-1}\Delta\sigma(\eta_{i,j+1}^{n+1}-\eta_{i,j}^{n+1})\\
&-(h_{i,j-1/2}^{n})^2\Delta\sigma^{\mathrm{T}}A_{i,j-1/2}^{-1}\Delta\sigma(\eta_{i,j}^{n+1}-\eta_{i,j-1}^{n+1})]\\
=\eta_{i,j}^{n}&-\frac{\delta t}{\delta x}[h_{i+1/2,j}^{n}(\Delta\sigma^{\mathrm{T}}A_{i+1/2,j}^{-1}G_{i+1/2,j})^{n}-h_{i-1/2,j}^{n}(\Delta\sigma^{\mathrm{T}}A_{i-1/2,j}^{-1}G_{i-1/2,j})^{n}]\\
&-\frac{\delta t}{\delta y}[h_{i,j+1/2}^{n}(\Delta\sigma^{\mathrm{T}}A_{i,j+1/2}^{-1}G_{i,j+1/2})^{n}-h_{i,j-1/2}^{n}(\Delta\sigma^{\mathrm{T}}A_{i,j-1/2}^{-1}G_{i,j-1/2})^{n}].
\end{aligned} \tag{37}$$

Here $\Delta\sigma^{\mathrm{T}}A^{-1}\Delta\sigma$ is a positive number. For each point (i, j) we thus have an equation for $\eta_{i,j}$, $\eta_{i+1,j}$, $\eta_{i,j+1}$, $\eta_{i-1,j}$ and $\eta_{i,j-1}$ giving a five-diagonal equation set. The resulting $I \times J$ equations are solved efficiently using a conjugate gradient solver. Having solved for η, the velocities u and v are obtained by solving the tridiagonal equations (31) and (32). The vertical velocity ω at the new time level $n+1$ may now be simply determined from (23) as

$$\begin{aligned}
\omega_{i,j,k+1/2}^{n+1} = \omega_{i,j,k-1/2}^{n+1} - \delta\sigma'\left(\frac{\partial\sigma}{\partial\sigma'}\right)_k\Bigg(&\frac{\eta_{i,j}^{n+1}-\eta_{i,j}^{n}}{\delta t}\\
&+\frac{h_{i+1/2,j}^{n+1}u_{i+1/2,j,k}^{n+1}-h_{i-1/2,j}^{n+1}u_{i-1/2,j,k}^{n+1}}{\delta x}+\frac{h_{i,j+1/2}^{n+1}u_{i,j+1/2,k}^{n+1}-h_{i,j-1/2}^{n+1}u_{i,j-1/2,k}^{n+1}}{\delta y}\Bigg).
\end{aligned} \tag{38}$$

The vertical velocity in physical space w may also be obtained from a finite difference form of (22) if needed.

The explicit operators Fu and Fv describing advection and horizontal diffusion remain to be defined. Also k and ε are needed to specify ν_{E} and c to determine ρ and hence the Boussinesq pressure gradient terms. k, ε and c are advanced in time alongside u, v and η: ν_{E} at time level n is used to advance u, v and η to time level $n+1$ which then provide the input to advance k, ε and c to time level $n+1$. As with u and v, for k, ε and c vertical diffusion is handled implicitly and advection, horizontal diffusion and source terms explicitly, lumped together into operators Fk, $F\varepsilon$ and Fc respectively. We now define their implicit time advancement in terms of Fk, $F\varepsilon$ and Fc which will be defined later along with Fu and Fv. k, ε are defined at vertical mesh points between those for u and v since this is most convenient for specifying ν_{E} for vertical diffusion which is considered a most important process in this study. c is also specified at the same points for convenience and since values at the bed and

surface are often needed. The numerical treatment of k, ε and c is thus the same apart from the source terms. We arbitrarily choose c to define the implicit component of equations (6), (7) and (9):

$$c^{n+1}_{i,j,k+1/2} = Fc^{n}_{i,j,k+1/2} + \delta t \frac{\dfrac{v^n_{i,j,k+1}}{\sigma_c}\left(\dfrac{\partial\sigma'}{\partial\sigma}\right)_{k+1}(c^{n+1}_{i,j,k+3/2} - c^{n+1}_{i,j,k+1/2}) - \dfrac{v^n_{i,j,k}}{\sigma_c}\left(\dfrac{\partial\sigma'}{\partial\sigma}\right)_{k}(c^{n+1}_{i,j,k+1/2} - c^{n+1}_{i,j,k-1/2})}{\delta\sigma'(h^n_{i,j})^2(\sigma_{k+1} - \sigma_k)}. \quad (39)$$

A tridiagonal matrix is formed for each horizontal position (i, j) which is solved to give k, ε and c. The boundary conditions for each are different and the matrix elements a_{lm} and the right-hand-side term b_l are now defined for c ($m = 1, \ldots, K+1$): for $m = 1$, corresponding to $k = \frac{1}{2}$, we require zero gradient, given by

$$a_{11} = 1, \qquad a_{12} = -1, \qquad b_1 = 0;$$

for $m = 2, \ldots, K$, corresponding to $k = \frac{3}{2}, \ldots, K - \frac{1}{2}$,

$$\begin{aligned} a_{m,m-1} &= -\delta t \frac{\dfrac{v_k}{\sigma_c}\left(\dfrac{\mathrm{d}\sigma'}{\mathrm{d}\sigma}\right)_k}{h^2_{i,j}\delta\sigma'(\sigma_{k+1} - \sigma_k)}, \\ a_{m,m} &= 1 + \delta t \frac{\dfrac{v_k}{\sigma_c}\left(\dfrac{\mathrm{d}\sigma'}{\mathrm{d}\sigma}\right)_k}{h^2_{i,j}\delta\sigma'(\sigma_{k+1} - \sigma_k)} + \delta t \frac{\dfrac{v_{k+1}}{\sigma_c}\left(\dfrac{\mathrm{d}\sigma'}{\mathrm{d}\sigma}\right)_{k+1}}{h^2_{i,j}\delta\sigma'(\sigma_{k+1} - \sigma_k)}, \\ a_{m,m+1} &= -\delta t \frac{\dfrac{v_{k+1}}{\sigma_c}\left(\dfrac{\mathrm{d}\sigma'}{\mathrm{d}\sigma}\right)_{k+1}}{h^2_{i,j}\delta\sigma'(\sigma_{k+1} - \sigma_k)}, \qquad b_m = Fc_{k+1/2}; \end{aligned} \quad (40)$$

for $m = K+1$, corresponding to $k = K + \frac{1}{2}$, we again require zero gradient, given by

$$a_{K+1,K} = -1, \qquad a_{K+1,K+1} = 1, \qquad b_{K+1} = 0.$$

For k and ε we only require $m = 1, \ldots, K$, corresponding to $k = \frac{3}{2}, K + \frac{1}{2}$, since values on the bed are not required and wall functions are used to specify magnitudes at $k = \frac{3}{2}$. For $m = 2, \ldots, K-1$ the elements of the tridiagonal matrix are as given by (40).

For k with $m = 1$ we require from (18)

$$a_{11} = 1, \qquad a_{12} = 0, \qquad b_1 = u_*^2/\sqrt{c_\mu}.$$

For $m = K$ without wind shear we have zero gradient, requiring

$$a_{K,K-1} = -1, \qquad a_{K,K} = 1, \qquad b_K = 0.$$

For ε with $m = 1$ we require from (19)

$$a_{11} = 1, \qquad a_{12} = 0, \qquad b_1 = u_*^3/\kappa h\sigma_{3/2}.$$

For $m = K$ we require from (20)

$$a_{K,K-1} = 0, \qquad a_{K,K} = 1, \qquad b_K = (k_{K+1/2}\sqrt{c_\mu})^{3/2}0{\cdot}07\kappa h.$$

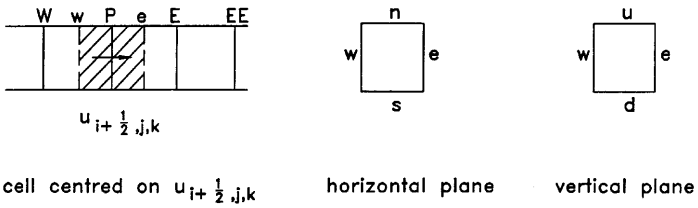

Figure 3. Sketch showing notation for advection scheme. The shaded area is the cell centred on $u_{i+1/2,\,j,k}$

We now define the explicit operators Fu and Fv, starting with the advective components Fu^{a} and Fv^{a}. To demonstrate the procedure, Figure 3 shows a cell centred on $u_{i+1/2,\,j,k}$ and from (24) the transport quantity $\phi = hu$. Fu^{a} is thus given by

$$Fu^{\mathrm{a}}_{i+1/2,\,j,k} = -\frac{\delta t}{h_{i+1/2,\,j}}\left(\frac{u_{\mathrm{e}}\phi_{\mathrm{e}} - u_{\mathrm{w}}\phi_{\mathrm{w}}}{\delta x} + \frac{v_{\mathrm{n}}\phi_{\mathrm{n}} - v_{\mathrm{s}}\phi_{\mathrm{s}}}{\delta y} + \frac{\omega_{\mathrm{u}}u_{\mathrm{u}} - \omega_{\mathrm{d}}u_{\mathrm{d}}}{\delta\sigma'(\partial\sigma/\partial\sigma')_{\mathrm{P}}}\right), \tag{41}$$

where u_{e}, u_{w}, v_{n}, v_{s}, ω_{u} and ω_{d} are obtained by linear interpolation, e.g.

$$u_{\mathrm{e}} = (u_{i+1/2,\,j,k} + u_{i+3/2,\,j,k})/2, \qquad v_n = (v_{i,\,j+1/2,k} + v_{i+1,\,j+1/2,k})/2,$$
$$\omega_u = (\omega_{i,\,j,k+1/2} + \omega_{i+1,\,j,k+1/2})/2,$$

and ϕ_{e}, ϕ_{w}, ϕ_{n}, ϕ_{s}, u_{u} and u_{d} are obtained from some upwind interpolation scheme. Here we use linear interpolation which is found to have good stability characteristics for this application and is second-order-accurate. This gives for ϕ_{e} for example

$$\text{for} \quad u_{\mathrm{e}} > 0, \quad \phi_{\mathrm{e}} = (3\phi_{\mathrm{P}} - \phi_{\mathrm{W}})/2, \qquad \text{for} \quad u_{\mathrm{e}} \leqslant 0, \quad \phi_{\mathrm{e}} = (3\phi_{\mathrm{E}} - \phi_{\mathrm{EE}})/2.$$

Note also that, to determine $\phi = uh$, h is also given by linear interpolation.

There is a corresponding scheme for Fv^{a} with $\phi = hv$.

The explicit components of Fu and Fv due to the Boussinesq pressure gradient terms Fu^{p} and Fv^{p} and horizontal diffusion terms Fu^{hd} and Fv^{hd} both require horizontal gradients in real space: of c for the former since $\rho = \rho(c)$ and of u and v for the latter. The method of calculation is the same in all cases. Consider Figure 4 where $\partial c/\partial x$ is required for $Fu^{\mathrm{p}}_{i+1/2,\,j,k}$. The horizontal level above datum at this position is

$$(1 + \sigma_k)h_{i+1/2,\,j} + z_{0i+1/2,\,j}.$$

The vertical distance from this level to the bed is required at $(i+1, j)$ to give c_2 and at (i, j) to give c_1 so that

$$\left(\frac{\partial c}{\partial x}\right)_{i+1/2,\,j,k} = \frac{c_2 - c_1}{\delta x}.$$

This vertical distance at $(i+1, j)$ is

$$(1 + \sigma_k)h_{i+1/2,\,j} + z_{0i+1/2,\,j} - z_{0i+1,\,j},$$

which is converted to σ' by (28). Putting

$$\frac{\sigma'}{\delta\sigma'} + 1 = n + \delta,$$

where n is an integer and $0 \leqslant \delta < 1$, gives by linear interpolation

$$c_2 = c_{i+1,\,j,n}(1 - \delta) + c_{i+1,\,j,n+1}\delta.$$

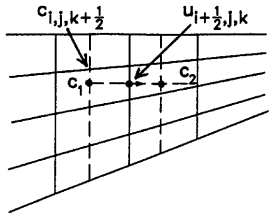

Figure 4. Sketch showing scheme for calculation of horizontal gradient $\partial c/\partial x$

c_1 is obtained in a similar way. If the position for c_1 or c_2 is below the bed or above the surface, $\partial c/\partial x$ is obtained by forward or backward differencing using c-values in the water. For example, if the position of c_1 is below the bed,

$$\left(\frac{\partial c}{\partial x}\right)_{i+1/2,\,j,k} = \frac{c_2 - c_{i+1/2,\,j,k}}{\delta x/2}.$$

$\partial c/\partial y$ is handled in a similar way.

The simple but effective still water test was made with a horizontal water surface, a sloping bed and density varying linearly with vertical distance below the surface, giving $\partial c/\partial x = 0$ everywhere. With a non-linear variation this would not be precisely zero and higher-order interpolation could be desirable for sharp density variations, however, this is not considered here.

Fu^{p} may now be obtained. From (12) we write

$$I = \frac{g}{\rho_0}\int_{z'=z}^{\eta} \frac{\partial \rho}{\partial x}\,\mathrm{d}z',$$

which is obtained numerically as

$$I_k = \frac{gh_{i+1/2,\,j}}{\rho_0}\left\{\left(\frac{\partial \rho}{\partial x}\right)_K(\sigma_{K+1/2} - \sigma_K) + \frac{1}{2}\sum_{l=k}^{K-1}\left[\left(\frac{\partial \rho}{\partial x}\right)_l + \left(\frac{\partial \rho}{\partial x}\right)_{l+1}\right](\sigma_{l+1} - \sigma_l)\right\},$$

giving

$$Fu^{\mathrm{p}}_{i+1/2,\,j,k} = -\delta t I_k.$$

Fu^{hd} may be specified with reference to Figure 5. In a finite volume approach the fluxes of $\nu_{\mathrm{E}}\partial u/\partial x$ through the vertical east and west cell faces and the fluxes of $\nu_{\mathrm{E}}\partial u/\partial y$ through the vertical north and

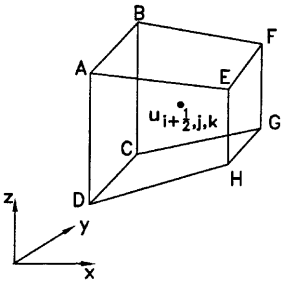

Figure 5. Notation for computation of horizontal diffusion for cell centred on $u_{i+1/2,\,j,k}$

south faces are required and these fluxes though the sloping upper and lower faces are also approximated, giving

$$
\begin{aligned}
&\frac{Fu^{\mathrm{hd}}_{i+1/2,\,j,k}\delta x\delta y\delta\sigma_k h_{i+1/2,\,j}}{\delta t}\\
&\quad=\left[\left(v_{\mathrm{E}}\frac{\partial u}{\partial x}\right)_{i+1,\,j,k}h_{i+1,\,j}-\left(v_{\mathrm{E}}\frac{\partial u}{\partial x}\right)_{i,\,j,k}h_{i,\,j}\right]\delta\sigma_k\delta y\\
&\qquad-\frac{1}{2}\left[\left(v_{\mathrm{E}}\frac{\partial u}{\partial x}\right)_{i+1,\,j,k+1/2}+\left(v_{\mathrm{E}}\frac{\partial u}{\partial x}\right)_{i,\,j,k+1/2}\right]\sigma_{k+1/2}(h_{i+1,\,j}-h_{i,\,j})\delta y\\
&\qquad+\frac{1}{2}\left[\left(v_{\mathrm{E}}\frac{\partial u}{\partial x}\right)_{i+1,\,j,k-1/2}+\left(v_{\mathrm{E}}\frac{\partial u}{\partial x}\right)_{i,\,j,k-1/2}\right]\sigma_{k-1/2}(h_{i+1,\,j}-h_{i,\,j})\delta y\\
&\qquad+\left[\left(v_{\mathrm{E}}\frac{\partial u}{\partial y}\right)_{i+1/2,\,j+1/2,k}h_{i+1/2,\,j+1/2}-\left(v_{\mathrm{E}}\frac{\partial u}{\partial y}\right)_{i+1/2,\,j-1/2,k}h_{i+1/2,\,j-1/2}\right]\delta\sigma_k\delta x\\
&\qquad-\frac{1}{2}\left[\left(v_{\mathrm{E}}\frac{\partial u}{\partial y}\right)_{i+1/2,\,j+1/2,k+1/2}+\left(v_{\mathrm{E}}\frac{\partial u}{\partial y}\right)_{i+1/2,\,j-1/2,k+1/2}\right]\sigma_{k+1/2}(h_{i+1/2,\,j+1/2}-h_{i+1/2,\,j-1/2})\delta x\\
&\qquad+\frac{1}{2}\left[\left(v_{\mathrm{E}}\frac{\partial u}{\partial y}\right)_{i+1/2,\,j+1/2,k-1/2}+\left(v_{\mathrm{E}}\frac{\partial u}{\partial y}\right)_{i+1/2,\,j-1/2,k-1/2}\right]\sigma_{k-1/2}(h_{i+1/2,\,j+1/2}-h_{i+1/2,\,j-1/2})\delta x.
\end{aligned}
\tag{42}
$$

In, for example, $v_{\mathrm{E}}\partial u/\partial x$ the suffices apply to v_{E} as well as $\partial u/\partial x$ for compactness. There is a corresponding expression for Fv.

The specification of Fu and Fv is now completed as

$$
Fu = u + Fu^{\mathrm{a}} + Fu^{\mathrm{p}} + Fu^{\mathrm{hd}}, \qquad Fv = v + Fv^{\mathrm{a}} + Fv^{\mathrm{p}} + Fv^{\mathrm{hd}}.
$$

We define the explicit advective operators Fk^{a}, $F\varepsilon^{\mathrm{a}}$ and Fc^{a} for the transport quantities $\phi = hk$, $h\varepsilon$ and hc in a similar way to Fu^{a} and Fv^{a}. Fc^{a} is used to demonstrate the procedure for a cell as shown in Figure 3 but centred on $c_{i,\,j,k+1/2}$, giving

$$
Fc^{\mathrm{a}}_{i,\,j,k+1/2} = -\frac{\delta t}{h_{i,j}}\left(\frac{u_{\mathrm{e}}\phi_{\mathrm{e}}-u_{\mathrm{w}}\phi_{\mathrm{w}}}{\delta x}+\frac{v_{\mathrm{n}}\phi_{\mathrm{n}}-v_{\mathrm{s}}\phi_{\mathrm{s}}}{\delta y}+\frac{\omega_{\mathrm{u}}c_{\mathrm{u}}-\omega_{\mathrm{d}}c_{\mathrm{d}}}{\delta\sigma'(\partial\sigma/\partial\sigma')_P}\right),
\tag{43}
$$

where u_{e}, u_{w}, v_{n}, v_{s}, ω_{u} and ω_{d} are obtained by linear interpolation, e.g.

$$
\begin{aligned}
u_{\mathrm{e}} &= (u_{i+1/2,\,j,k}+u_{i+1/2,\,j,k+1})/2, \qquad v_{\mathrm{n}} = (v_{i,\,j+1/2,k}+v_{i,\,j+1/2,k+1})/2,\\
\omega_{\mathrm{u}} &= (\omega_{i,\,j,k+1/2}+\omega_{i,\,j,k+3/2}/2,
\end{aligned}
$$

and ϕ_{e}, ϕ_{w}, ϕ_{n}, ϕ_{s}, c_{u} and c_{d} are obtained from the linear upwind interpolation scheme. As before, to determine $\phi = hc$, h is also obtained by linear interpolation.

Fc^{hd} is specified following the same procedure as for Fu^{hd} and Fv^{hd}:

$$\begin{aligned}
&\frac{Fc^{\mathrm{hd}}_{i,j,k+1/2}\delta x\delta y\delta\sigma_{k+1/2}h_{i,j}}{\delta t}\\
&=\left[\left(v_{\mathrm{E}}\frac{\partial c}{\partial x}\right)_{i+1/2,j,k+1/2}h_{i+1/2,j}-\left(v_{\mathrm{E}}\frac{\partial c}{\partial x}\right)_{i-1/2,j,k+1/2}h_{i-1/2,j}\right]\delta\sigma_{k+1/2}\delta y\\
&\quad-\frac{1}{2}\left[\left(v_{\mathrm{E}}\frac{\partial c}{\partial x}\right)_{i+1/2,j,k+1}+\left(v_{\mathrm{E}}\frac{\partial c}{\partial x}\right)_{i-1/2,j,k+1}\right]\sigma_{k+1}(h_{i+1/2,j}-h_{i-1/2,j})\delta y\\
&\quad+\frac{1}{2}\left[\left(v_{\mathrm{E}}\frac{\partial c}{\partial x}\right)_{i+1/2,j,k}+\left(v_{\mathrm{E}}\frac{\partial c}{\partial x}\right)_{i-1/2,j,k}\right]\sigma_{k}(h_{i+1/2,j}-h_{i-1/2,j})\delta y\\
&\quad+\left[\left(v_{\mathrm{E}}\frac{\partial c}{\partial y}\right)_{i,j+1/2,k+1/2}h_{i,j+1/2}-\left(v_{\mathrm{E}}\frac{\partial c}{\partial y}\right)_{i,j-1/2,k+1/2}h_{i,j-1/2}\right]\delta\sigma_{k+1/2}\delta x\\
&\quad-\frac{1}{2}\left[\left(v_{\mathrm{E}}\frac{\partial c}{\partial y}\right)_{i,j+1/2,k+1}+\left(v_{\mathrm{E}}\frac{\partial c}{\partial y}\right)_{i,j-1/2,k+1}\right]\sigma_{k+1}(h_{i,j+1/2}-h_{i,j-1/2})\delta x\\
&\quad+\frac{1}{2}\left[\left(v_{\mathrm{E}}\frac{\partial c}{\partial y}\right)_{i,j+1/2,k}+\left(v_{\mathrm{E}}\frac{\partial c}{\partial y}\right)_{i,j-1/2,k}\right]\sigma_{k}(h_{i,j+1/2}-h_{i,j-1/2})\delta x.
\end{aligned}\tag{44}$$

There are corresponding expressions for Fk^{hd} and $F\varepsilon^{\mathrm{hd}}$.

The source terms for solute transport are simply specified here at one or more cells as a concentration or an inflow of solute. The source terms for k and ε transport, Fk^{s} and $F\varepsilon^{\mathrm{s}}$, both involve the production term P (equations (6)–(8)). This is now written in full for completeness:

$$\begin{aligned}
P=v_{\mathrm{E}}\Bigg[&2\left(\frac{\partial u}{\partial x}\right)^2+\left(\frac{\partial v}{\partial x}+\frac{\partial u}{\partial y}\right)\frac{\partial v}{\partial x}+\left(\frac{\partial w}{\partial x}+\frac{\partial u}{\partial z}\right)\frac{\partial w}{\partial x}+\left(\frac{\partial u}{\partial y}+\frac{\partial v}{\partial x}\right)\frac{\partial u}{\partial y}+2\left(\frac{\partial v}{\partial y}\right)^2\\
&+\left(\frac{\partial w}{\partial y}+\frac{\partial v}{\partial z}\right)\frac{\partial w}{\partial y}+\left(\frac{\partial u}{\partial z}+\frac{\partial w}{\partial x}\right)\frac{\partial u}{\partial z}+\left(\frac{\partial v}{\partial z}+\frac{\partial w}{\partial y}\right)\frac{\partial v}{\partial z}+2\left(\frac{\partial w}{\partial z}\right)^2\Bigg].
\end{aligned}\tag{45}$$

The horizontal velocity gradients are calculated in real space and

$$\frac{\partial}{\partial z}=\frac{1}{h}\frac{\partial}{\partial\sigma'}\frac{\partial\sigma'}{\partial\sigma}.$$

We thus have

$$\begin{aligned}
Fk^{\mathrm{s}}_{i,j,k+1/2}&=\delta t(P_{i,j,k+1/2}-\varepsilon_{i,j,k+1/2}),\\
F\varepsilon^{\mathrm{s}}_{i,j,k+1/2}&=\delta t\left(c_{1\varepsilon}\frac{\varepsilon_{i,j,k+1/2}}{k_{i,j,k+1/2}}P_{i,j,k+1/2}-c_{2\varepsilon}\frac{\varepsilon^2_{i,j,k+1/2}}{k_{i,j,k+1/2}}\right)
\end{aligned}\tag{46}$$

and

$$\begin{aligned}
Fc&=c+Fc^{\mathrm{a}}+Fc^{\mathrm{hd}}+Fc^{\mathrm{s}},\\
Fk&=k+Fk^{\mathrm{a}}+Fk^{\mathrm{hd}}+Fk^{\mathrm{s}},\\
F\varepsilon&=\varepsilon+F\varepsilon^{\mathrm{a}}+F\varepsilon^{\mathrm{hd}}+F\varepsilon^{\mathrm{s}}.
\end{aligned}$$

The numerical scheme is thus complete apart from consideration of boundary conditions, wetting and drying and laminar/turbulent transition near a wet/dry boundary which are described below.

4. RESULTS

Although the aim is to produce a general solver for tidal and estuarial flows, it is valuable to consider first parallel oscillatory flow to compare with existing solutions and field data. In this context a detailed study of the oscillatory bed boundary layer has been made by Justesen.[12] This is usually driven by periodic surface waves and is different from oscillatory tidal flow in that the free surface is effectively at infinity with an outer boundary condition ($z \rightarrow \infty$) given by

$$\frac{1}{\rho}\frac{\partial p}{\partial x} = -\frac{\partial u_\infty}{\partial t}, \tag{47}$$

where $u_\infty = u_M \sin(2\pi t/T)$ in this case; T is the flow period and u_M is the amplitude of u_∞. The rough turbulent boundary layer is considered which is defined only by A/k_s, where $A = u_M T/2\pi$ is the amplitude of particle motion (outside the boundary layer). Justesen presented detailed information for $A/k_s = 1000$, including contour plots of k/u_M^2 and l/k_s on a (z/A)–(t/T) plane. l is a representative turbulence length scale given by the formula for isotropic turbulence $l = c_\mu k^{3/2}/\varepsilon$ which has a simpler physical interpretation than ε. Contour plots of k/u_M^2 and l/k_s from the general code developed here, stripped down to 1D (in the vertical), are shown in Figures 6 and 7. These are very close to those presented by Justesen and were obtained with the following numerical parameters: $\delta t/T = 0{\cdot}002$, the free surface $0{\cdot}25A$ above the bed, 100 cells and a bed cell size of $0{\cdot}23k_s$ giving 28 cells across depth presented in Figures 6 and 7. These results were insensitive to refining further the numerical discretization (reducing the number of cells below 40 started to give a marked deviation). It is clearly seen how k and l vary temporally and spatially, indicating that such a two-equation model is necessary for oscillatory flow predictions. Whether the eddy viscosity assumption is adequate can be inferred from the predictions of velocity variation and bed shear stress. Justesen made a detailed

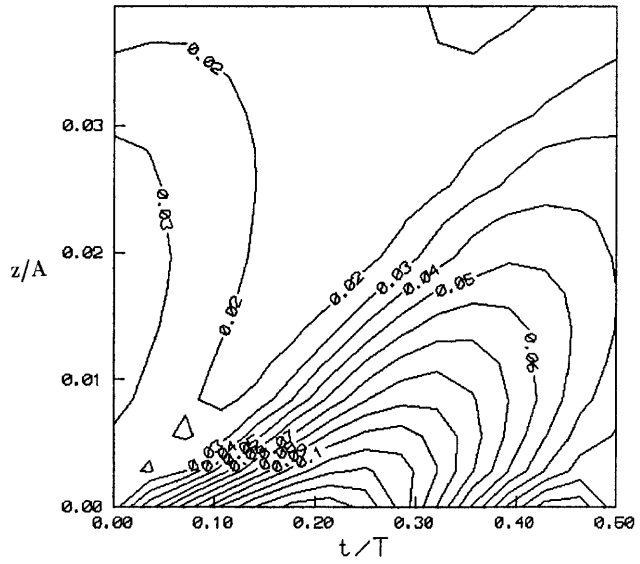

Figure 6. Contour plot of $10k/u_M^2$ on (z/A)–(t/T) plane for wave-induced bed boundary layer with $A/k_s = 1000$

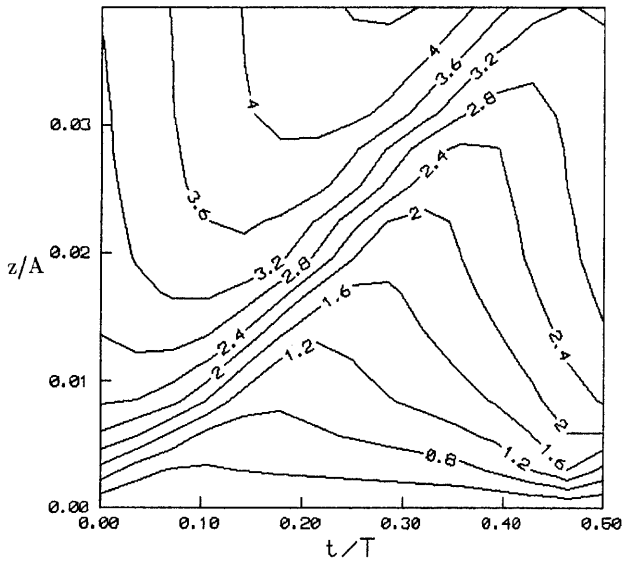

Figure 7. Contour plot of l/k_s on (z/A)–(t/T) plane for wave-induced bed boundary layer with $A/k_s = 1000$

comparison with several experimental studies and concluded that the turbulence and flow characteristics were well predicted by this model, apart from the level of turbulence energy very close to the bed (within one to two roughness heights). The bed shear stress is well predicted so by implication the turbulence dissipation rate is also not well predicted in this narrow region. However, the distinct differences between the acceleration and deceleration phases are captured and the spreading of turbulence from the near-wall region with high production to the outer boundary layer is fully accounted for. This is of course important for the accurate prediction of mixing processes. Although the good prediction of bed shear stress is in fact not a severe test since simpler theories provide similar predictions, the overall predictions by the two-equation model represent a considerable improvement.

We are fortunate in having some field data available and comparisons are made following Baumert and Radach.[15] Figures 8 and 9 compare time variations of velocity and turbulence kinetic energy from the Elbe estuary. The water depth was 5·1 m, the tidal period was 12 h 25 min, the roughness height was 0·02 m and the measurements were made at a level of about 1·9 m from the bed. The driving pressure gradient was estimated to be given by

$$-\frac{1}{\rho}\frac{\partial p}{\partial x} = gS_M \cos\left(\frac{2\pi t}{T}\right), \tag{48}$$

where S_M is a maximum surface slope of 5×10^{-5} in this case. Results were obtained with 4000 time steps per period, 100 cells and a bed cell size of 0·032 m ($a = 0{\cdot}196$ in equation (28)) and agreement with field data for u and k is seen to be satisfactory.

Time variations of velocity and bed shear stress for the Jade estuary are shown in Figures 10 and 11. Here the water depth is rather greater at about 20 m, the roughness height is smaller at 0·002 m and S_M is estimated to be 2×10^{-5}. The measurements were made at a distance of 2·14 m from the bed. The computed results were obtained with 100 cells, a bed cell size of 0·005 m ($a = 0{\cdot}002$) and 20,000 time steps per period. The agreement of velocity with experiment is reasonable but the computed bed shear stress gives an upper bound to the measurements and is slightly greater than the

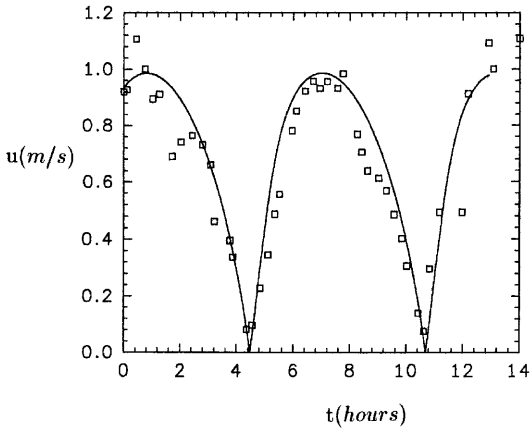

Figure 8. Variation of velocity u (m s^{-1}) at 1·9 m above bed with time for Elbe estuary: ————, computed; □, measured

values computed by Baumert and Radach. They, however, used a regular mesh with 50 cells and to demonstrate mesh independence the results here were recomputed with a bed cell size of 0·018 m ($a = 0{\cdot}01$). The results were virtually identical. All results presented are independent of further refinement of numerical parameters. Interestingly the maximum $Re_{*0} = u_* \delta z_0 / v$ where δz_0 is the bed cell size, was 113 for the former and 409 for the latter. Strictly the wall functions are only valid for $Re_* < 100$ but this limit would appear not to be too significant for these flows. Finally the time steps used here to produce stable results were very much smaller than those of Baumert and Radach, probably because of the very much smaller cell size at the bed in these computations.

To demonstrate the influence of water depth for the three cases, the variations of bed shear stress with time are shown in Figure 12. The effect of water depth on phase from the shallow Elbe case to the deeper Jade case and then to the effectively infinite-depth bed boundary layer case is most marked. This is further emphasized by the contour plots of k and l for the Elbe, shown in Figures 13 and 14, and the Jade, shown in Figures 15 and 16. For the shallow Elbe the length scale is fairly constant with time, except when the bed shear stress is near zero. For the deeper Jade case there is

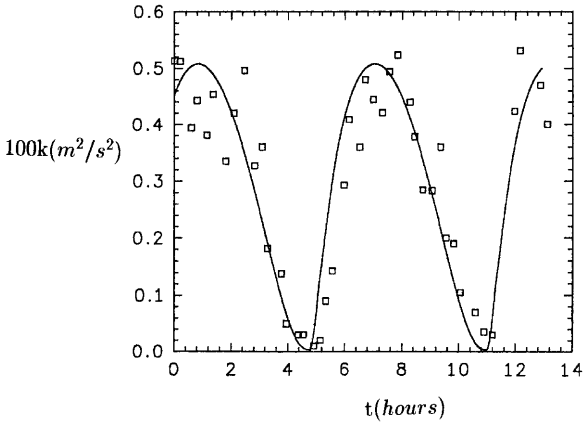

Figure 9. Variation of turbulent kinetic energy $100k$ (m^2 s^{-2}) at 1·9 m above bed with time for Elbe estuary: ————, computed; □, measured

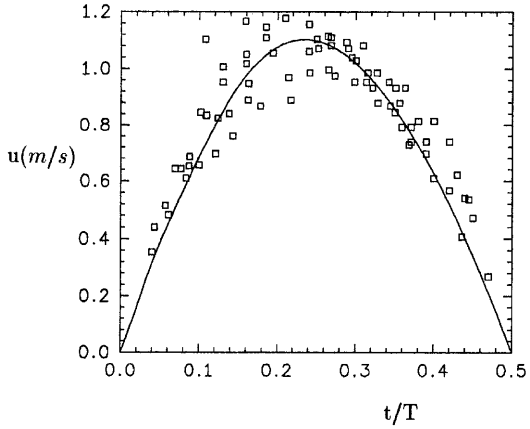

Figure 10. Variation of velocity u (m s^{-1}) at 2·14 m above bed with time for Jade estuary: ————, computed; □, measured

more variation and in both cases the k contours have a similar shape relative to the time of zero bed shear stress. Both k and l are quite different from the infinite-depth case shown in Figures 6 and 7. Clearly the influence of water depth on k and l and hence eddy viscosity is complex and further demonstrates the desirability of a two-equation turbulence model for computing general flow situations and mixing processes.

These 1D runs were made on a 486 PC requiring a few minutes at most and are a very convenient way of establishing numerical parameters needed for stability and accuracy of vertical processes prior to time-consuming 3D computations. The 1D cases often provide the limiting criteria when transferred to general 3D problems.

To demonstrate 3D flow prediction, computations of flow around a conical island with gently sloping sides are made and compared with the laboratory experiments.[2] Results are available for steady ambient current flow at present. The experimental configuration is shown in Figure 17. The first test is made with an island side slope $\theta = 22^\circ$ where some laser Doppler anemometer (LDA) velocity measurements are available. This test case was also used by Stansby and Lloyd[9] where the numerical model incorporated Lagrangian advection and a simple two-layer mixing length turbulence model. The scheme of Stansby and Lloyd for wetting and drying is used again here with a cut-off

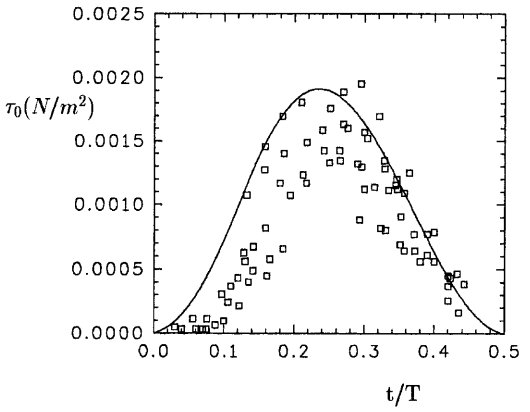

Figure 11. Variation of bed shear stress τ_0 (N m^{-2}) with time for Jade estuary: ————, computed; □, measured

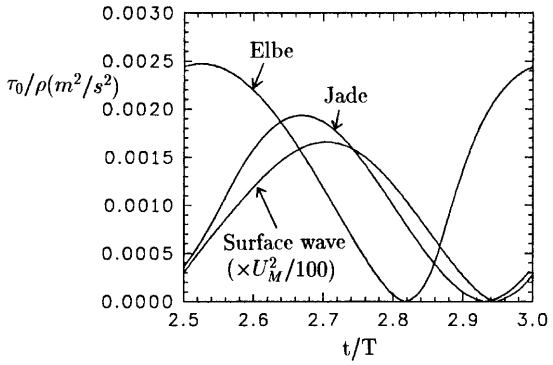

Figure 12. Variation of bed shear stress τ_0/ρ ($m^2\ s^{-2}$) with time for wave-induced bed boundary layer, Elbe estuary and Jade estuary

depth of $\delta x \tan\theta$ below which a cell is said to be dry. Close to a wet/dry boundary we also allow transition to laminar flow as the boundary is approached. For $Re_h = u_m h/v > 1000$ the flow is said to be fully turbulent and for $Re_h < 500$ (values typical of steady channel flows) fully laminar, with eddy viscosity and turbulence characteristics taking a linearly weighted average of the turbulent value and the laminar value between these limits. This is obviously rather idealized physically but it affects a small area close to the boundary and is desirable for numerical stability. The initial conditions are those of still water and the inlet velocity is increased as a quarter sinusoid (with a period of 20 or 40 s in the computations below) up to the required onset velocity. The turbulence characteristics for steady channel flow are also set at the inlet, based on mean inlet velocity. At the outlet the velocities and scalar quantities are given zero normal gradients. This condition is sufficiently far downstream to have negligible effect on the results presented.[9] The side walls of the flume are treated as slip boundaries. In the experiment the boundary layer is smooth turbulent and the roughness height in the

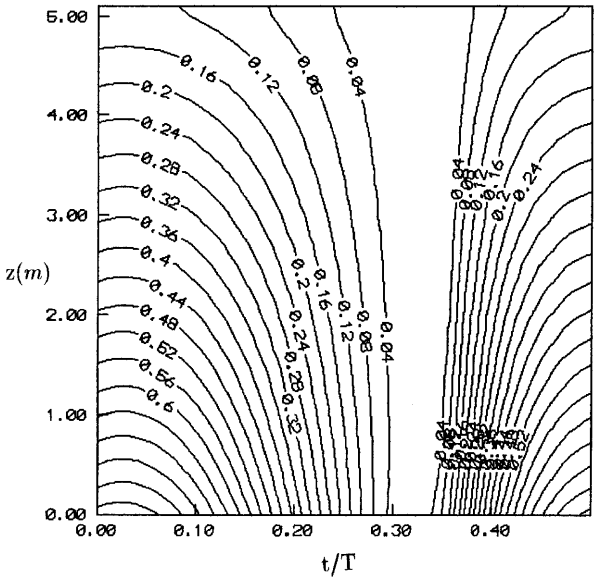

Figure 13. Contour plot of $100k$ ($m^2\ s^{-2}$) on z–(t/T) plane for Elbe estuary

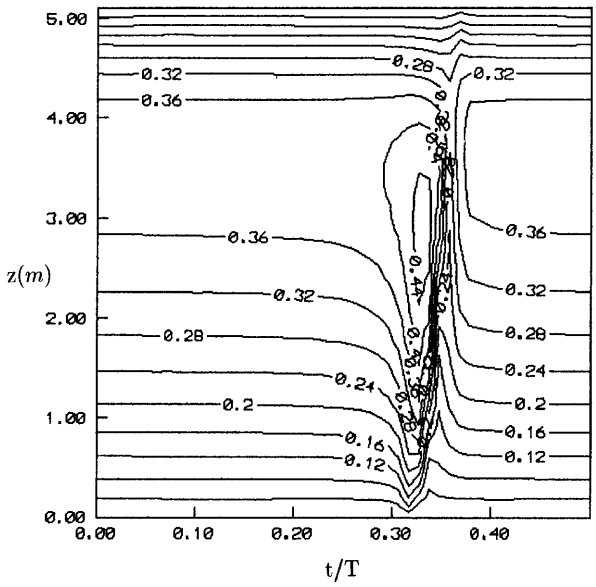

Figure 14. Contour plot of l (m) on z–(t/T) plane for Elbe estuary

model is adjusted to give the same bed shear stress in the ambient flow ($k_s = 0{\cdot}00022$ m). Variations of u- and v-velocity with time are shown in Figure 18 for the two horizontal positions shown in Figure 17, one some distance away from the wake centreline and one close to the wake centreline (Figures 18(a) and 18(b) respectively). The vertical measurement position is just below the surface. A $163 \times 51 \times 20$ mesh was used with 0·0304 m horizontal mesh size ($\delta x = \delta y$) and a vertical

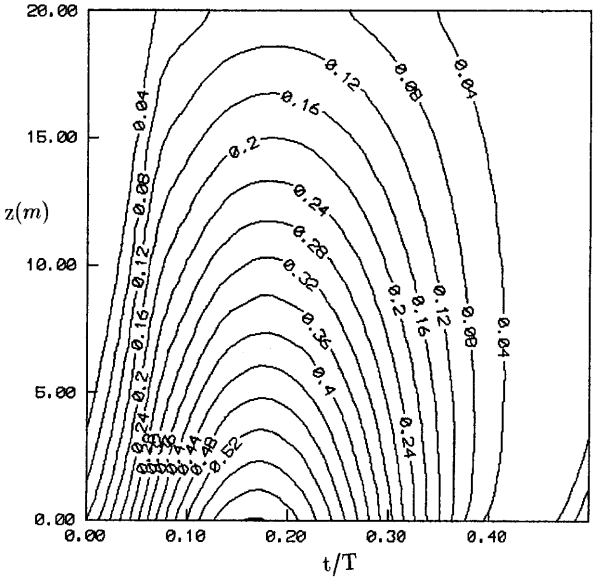

Figure 15. Contour plot of $100k$ (m^2 s^{-2}) on z–(t/T) plane for Jade estuary

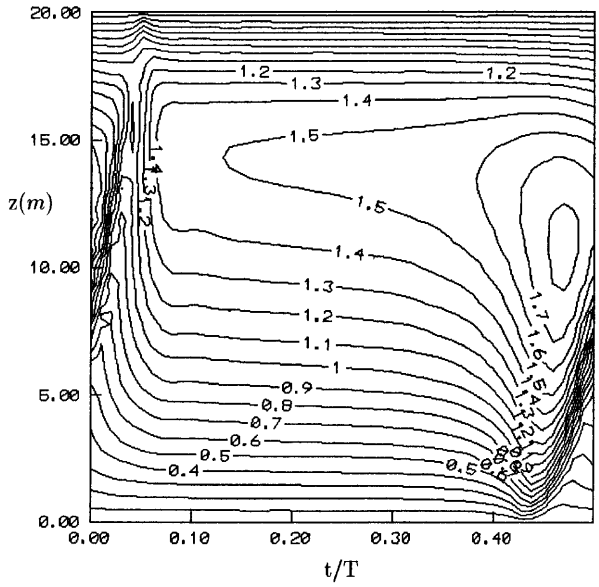

Figure 16. Contour plot of l (m) on z–(t/T) plane for Jade estuary

mesh spacing at the bed of 0·0004 m ($a = 0{\cdot}001$) in the ambient flow where the mean velocity is 0·088 m s^{-1} and the depth is 0·08 m. A time step δt of 0·01 s was used. The wake became asymmetric and produced vortex shedding without any imposed asymmetry. At the position away from the wake centreline the mean and fluctuating u-velocity components are in reasonable agreement with experiment, although the dominant frequency is about 15% higher. There are no corresponding LDA measurements of the v-velocity. This computation was repeated on an $81 \times 25 \times 20$ mesh with a horizontal mesh size of 0·0608 m and the same vertical mesh. The corresponding velocity time variations are shown in Figure 19 to be similar, although the dominant frequency is now only 10% higher than the LDA measurements and the magnitude of the v-velocity fluctuations is almost halved for both positions, indicating less vigorous vortex shedding.

Comparisons of solute transport computations with experimental dye visualization were made with the 8° slope island. Comparisons are qualitative and cases with two stability parameters ($S = C_f D/h$) of 0·06 and 0·35 with vigorous and weak eddy shedding respectively are shown in Figures 20 and 21. C_f is the coefficient of friction and D is the island diameter at mid-depth.[2] The point in the vortex-shedding cycle was chosen to be equivalent to that shown for the dye visualization. The more refined

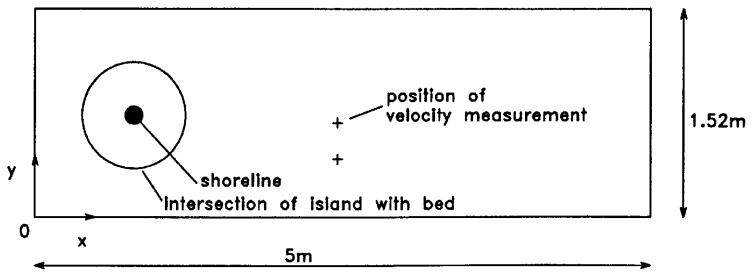

Figure 17. Sketch of flume and island configuration (with 22° side slope)

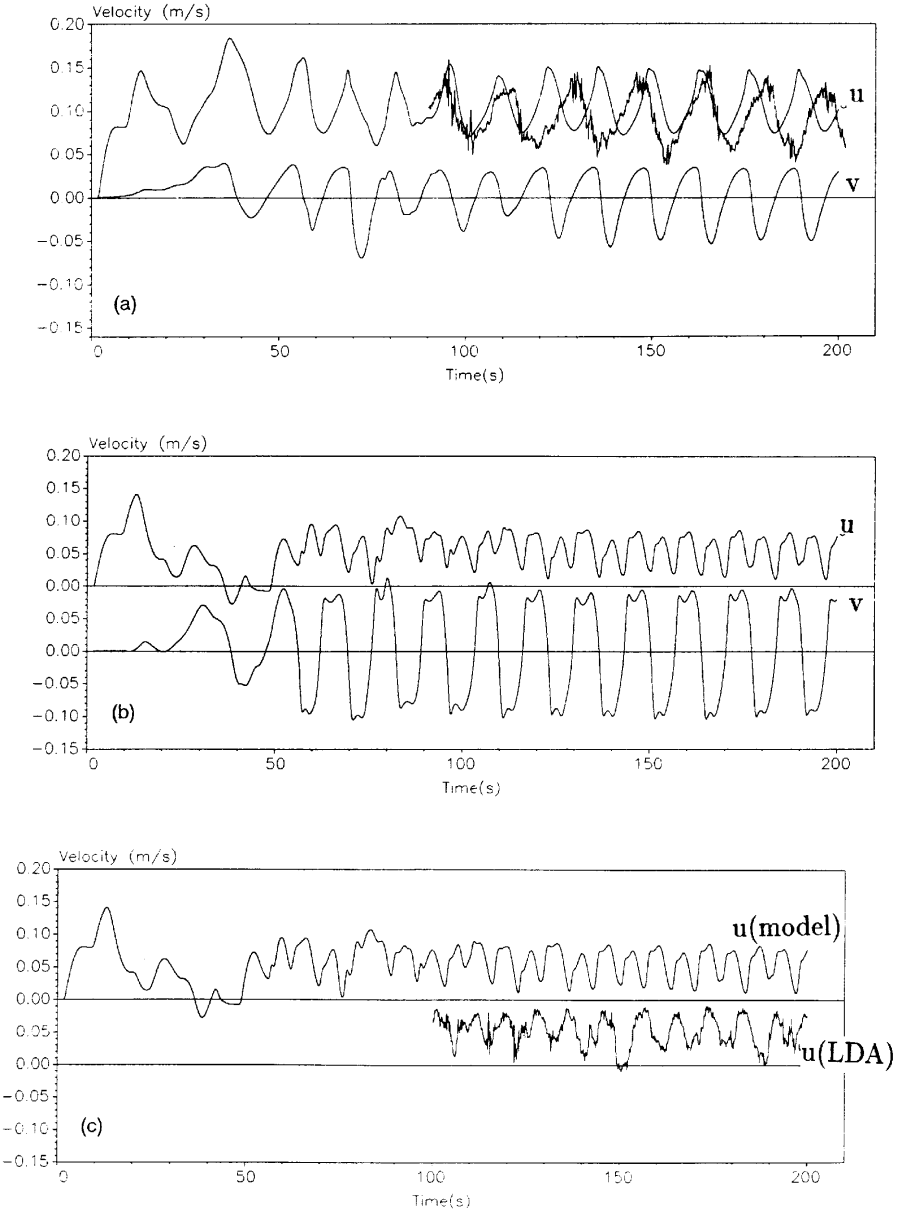

Figure 18. Variations of u- and v-velocity (m s^{-1}) with time for positions shown in Figure 17 for island with 22° side slope. The spiky plot (indicating turbulence) shows the LDA measurement. The computational mesh size is $163 \times 51 \times 20$. (a) At $x = 1{\cdot}62$ m, $y = 0{\cdot}45$ m, computed and LDA. (b) At $x = 1{\cdot}62$ m, $y = 0{\cdot}73$ m, computed. (c) At $x = 1{\cdot}62$ m, $y = 0{\cdot}73$ m, u-component only, computed and LDA

$163 \times 51 \times 20$ mesh was used and it can be seen how at least the gross wake structures are captured in both cases. The solute was input in one cell at mid-depth just downstream of the island. Computed contours at the surface, mid-depth and the bed are shown in Figures 20 and 21. Those at mid-depth and the surface are very similar and also at the bed for $S = 0{\cdot}35$ indicating the two-dimensionality of the wake.

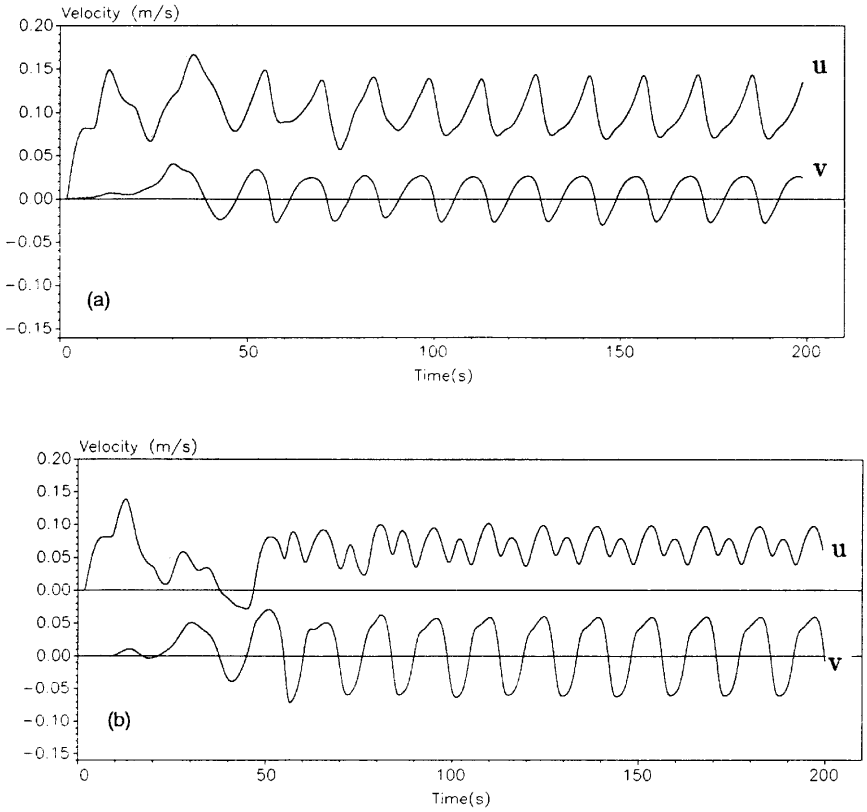

Figure 19. As Figure 18 with computational mesh size of 81 × 25 × 20. Computed velocities only. (a) At $x = 1{\cdot}62$ m, $y = 0{\cdot}45$ m. (b) At $x = 1{\cdot}62$ m, $y = 0{\cdot}73$ m

Finally the configuration with $S = 0{\cdot}06$ is used to demonstrate the influence of temperature on the input solute. The ambient temperature is set at 15°C and the input again in one cell is now upstream of the island, slightly offset from the centreline, at mid-depth. The same initial flow conditions are used in all cases and the influence of the plume on the flow is very small, as inferred from velocity time histories. Again no flow asymmetry was imposed. Temperature contours with a solute input temperature of 16°C (almost neutrally buoyant) are shown in Figure 22. The contour magnitudes show the temperature difference from ambient. In all cases so far linear upwind interpolation (second-order-accurate) has been used. The same case is shown with a third-order-accurate flux-limited upwind scheme[17–19] in Figure 23 and the contours are very similar though not identical. This aspect will be pursued further elsewhere particularly in relation to suspended sediment transport and Figure 23 is included here to demonstrate the insensitivity of solute transport to a higher-order scheme.

The case with a solute input temperature of 30°C is shown in Figure 24 (with linear upwind interpolation). The hotter solute tends to move upwards in general as would be expected. However, the situation is clearly complex and this result is only for one instant in time. A detailed investigation with experimental measurements is desirable.

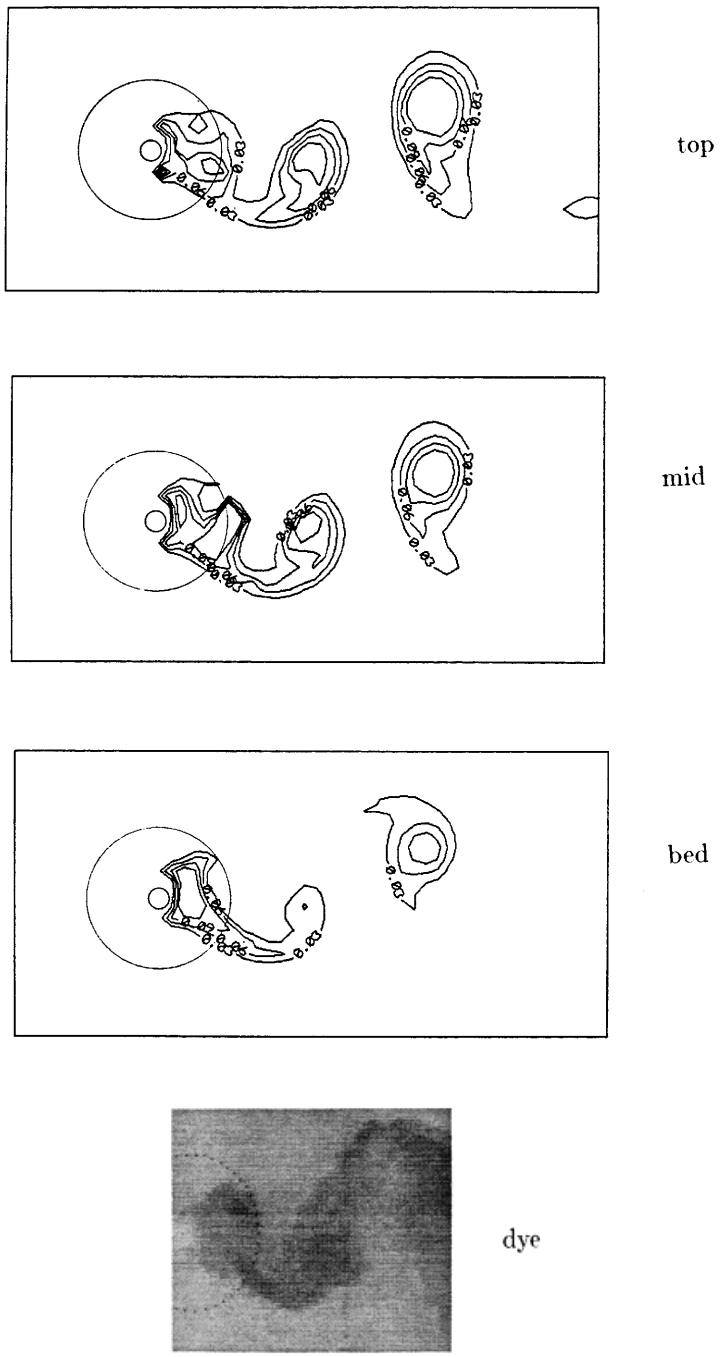

Figure 20. Computed concentration contours at surface, mid-depth and bed at $t = 150$ s and experimental dye visualization for 8° slope island with mean ambient velocity of 0·115 m s^{-1} and depth of 0·045 m (giving a stability parameter $S = 0{\cdot}06$)

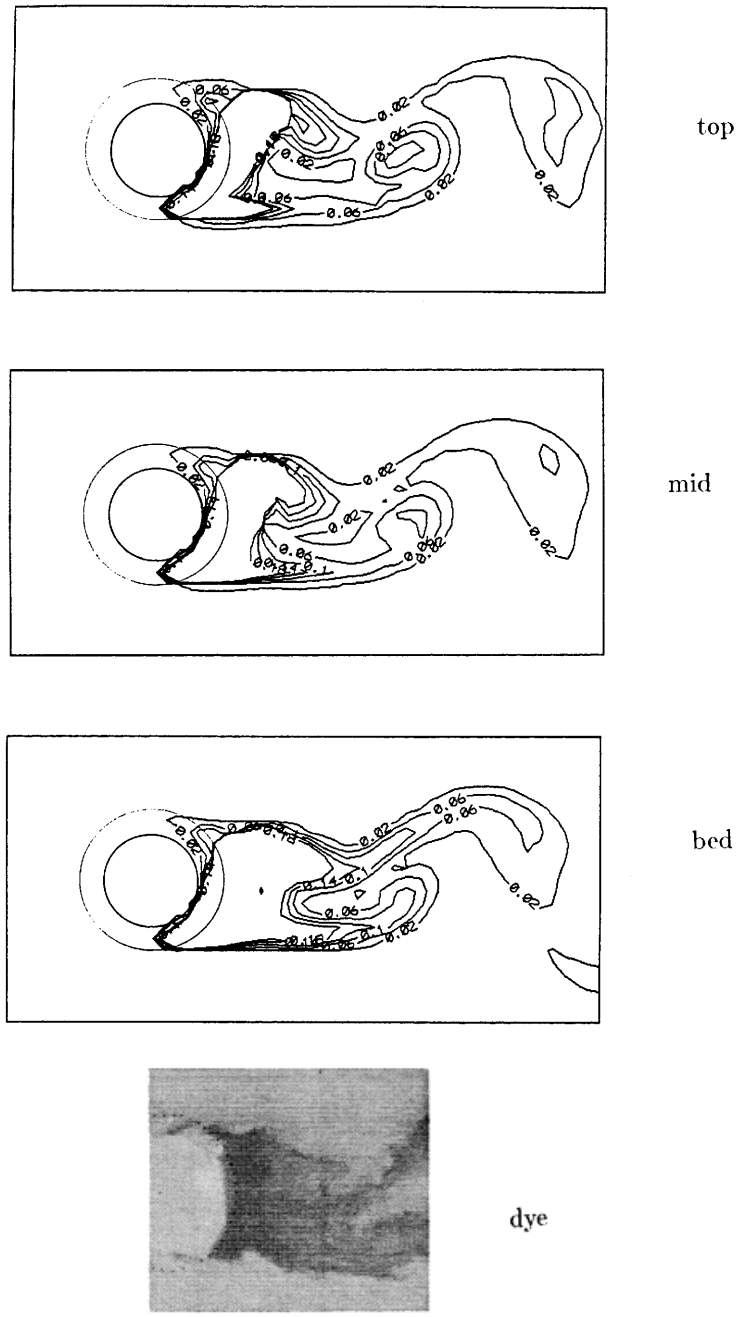

Figure 21. Computed concentration contours at surface, mid-depth and bed at $t = 150$ s and experimental dye visualization for 8° slope island with mean ambient velocity of 0·1 m s^{-1} and depth of 0·016 m (giving a stability parameter $S = 0{\cdot}35$)

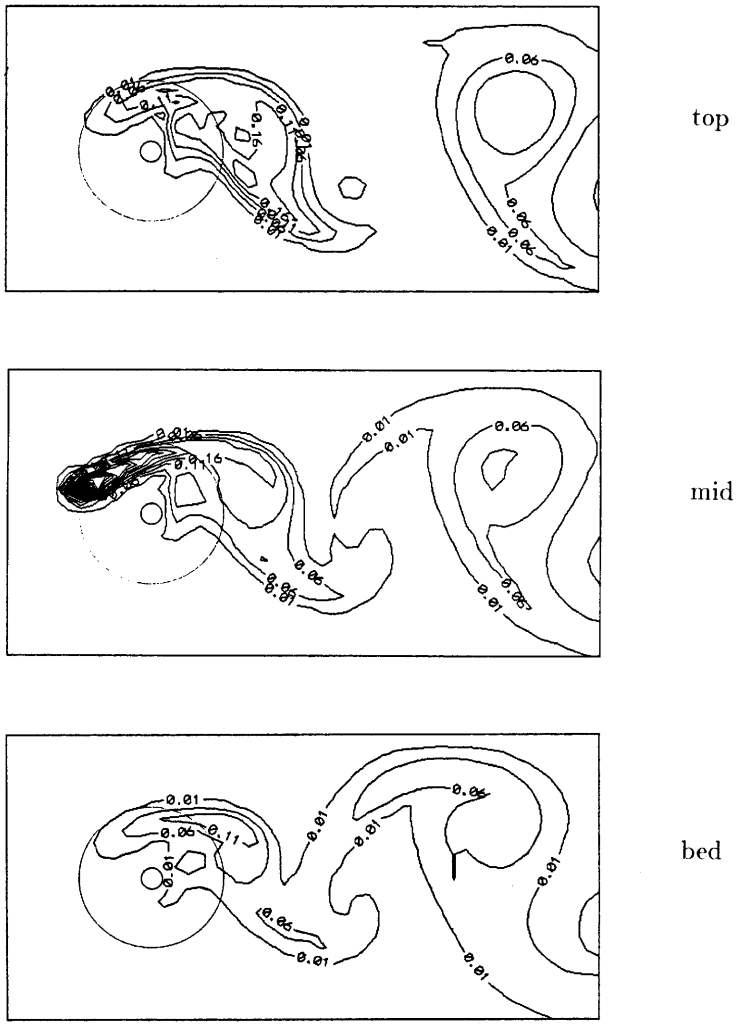

Figure 22. Computed contours of temperature difference (local minus ambient) at surface, mid-depth and bed for 8° slope island with mean ambient velocity of 0·115 m s^{-1} and depth of 0·045 m (giving a stability parameter $S = 0{\cdot}06$). The temperature of solute input is 16°C and the ambient temperature is 15°C. The contours have a 0·05°C temperature spacing

5. DISCUSSION AND CONCLUSIONS

A conservative finite volume scheme for 3D shallow-water flow with k–ε turbulence modelling and non-neutrally buoyant solute dispersion has been presented. The k–ε model may be considered the minimum level of turbulence model required for oscillatory flows, although simple mixing length models give good predictions of bed shear stress. 1D vertical computations for parallel oscillatory tidal flows show good (though limited) predictions of field measurements of velocity, bed shear stress and turbulence energy k. However, solute dispersion is likely to be more sensitive to turbulence quantities and this remains to be assessed. The difference in turbulence characteristics between the depths of 5 m (in the Elbe estuary) and 20 m (in the Jade estuary) is quite marked.

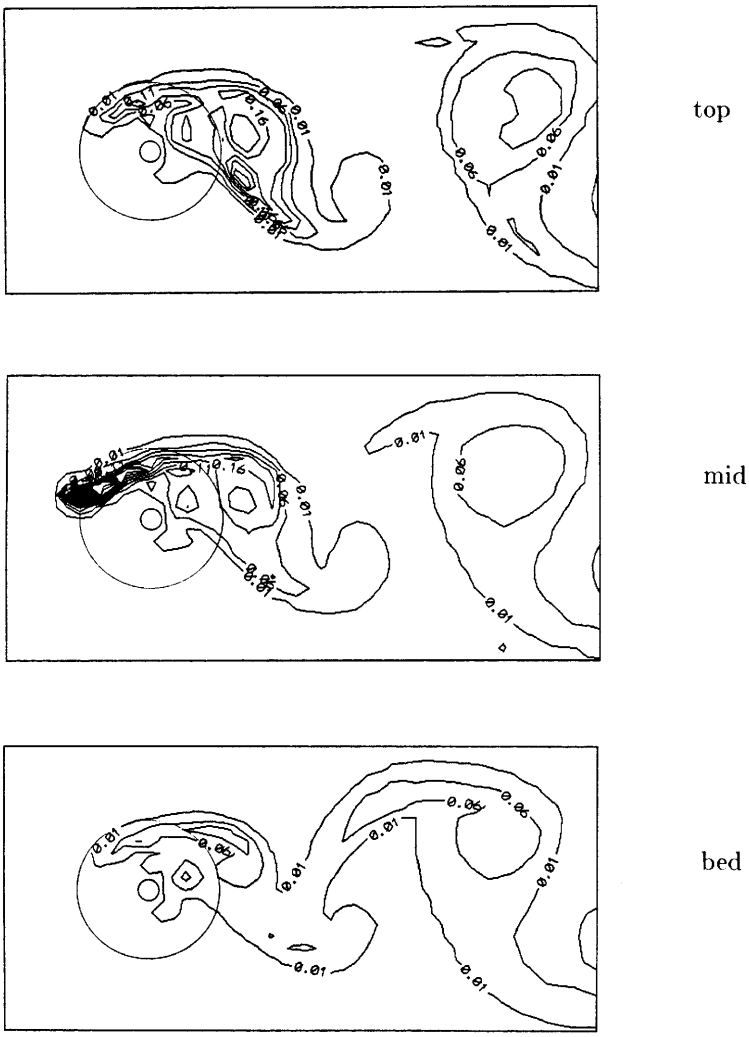

Figure 23. As Figure 22 with Van Leer's third-order flux-limited upwind interpolation scheme for solute advection

The conservative scheme is particularly desirable for scalar transport and is preferred to the non-conservative Lagrangian scheme used previously by the author.[9] This entails the use of upwind interpolation for advection and the linear approximation giving second-order accuracy has shown good stability characteristics in the study of flow around an island of small side slope with vortex shedding, which may be considered a severe test. Limited tests with a third-order-accurate flux-limited scheme (for momentum as well as scalar quantities) were less robust and were not pursued further. The use of this higher-order scheme for solute transport, however, gave very similar results for the one case investigated.

A widely recognized consequence of using k–ε modelling is the need for a smaller time step than for algebraic mixing length models. Here a time step of about one-fifth of that required with a mixing length model with Lagrangian advection[9] was required for the island study. However, reasonable agreement with experiment was obtained here with a larger (horizontal) mesh size.

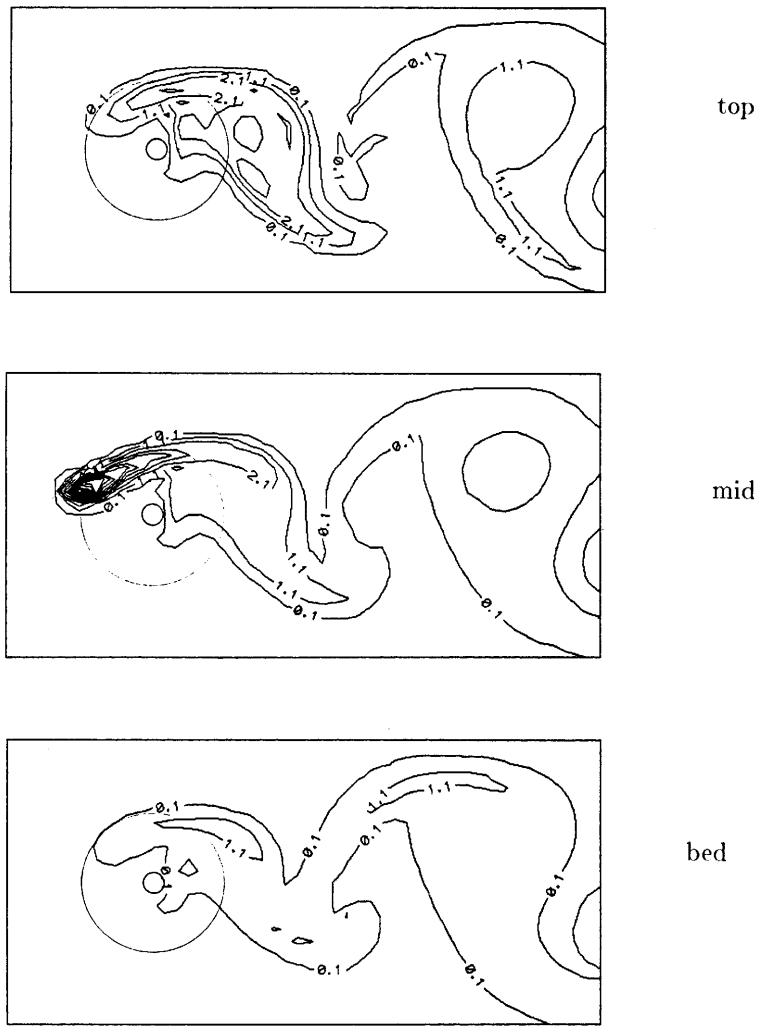

Figure 24. As Figure 22 (with linear upwind interpolation). The temperature of solute input is 30°C and the ambient temperature is 15°C. The contours have a 1°C temperature spacing

The computations were made on a Dec Alpha 600 workstation and one time step for the $163 \times 51 \times 20$ mesh required about 9 s computing time. Large-scale 3D computations are thus a practical proposition on such a modern workstation.

In such a scheme the computational effort in solving for surface elevation in a fully coupled way by a conjugate gradient solver is a very small proportion of the time step. Most effort goes into generating the matrix components of the wet cells before solution and then computing desired quantities after solution. For many cases there would thus appear to be little advantage in boundary-fitted meshes for 3D flows since dry cells represent little overhead, probably less than that associated with the additional algebra for a non-rectangular mesh. However, for coastal problems extending from deep water to confined estuaries a variable mesh size could be an advantage and should be a subject for further effort.

The uncertainty in the prediction of solute dispersion in oscillatory flow with k–ε modelling has been mentioned. Comparisons with controlled experiments would be highly desirable and also with full Reynolds stress transport modelling. For the case of vortex shedding from an island, aspects associated with non-hydrostatic pressure are worthy of computational investigation as discussed by Lloyd and Stansby.[2] The combination of recirculating flows around islands and headlands within tidal oscillations remains an important validation exercise to be undertaken. Finally the influence of solute temperature or density on turbulence structures is poorly understood and has been ignored here. The limited results presented indicate the complexity of the phenomena in recirculating flows.

ACKNOWLEDGEMENT

The Dec Alpha 600 workstation was provided on EPSRC grant GRK95666 and this is gratefully acknowledged.

REFERENCES

1. J. J. Leendertse, 'Aspects of a computational model for long period wave propagation', *Memo RM-5294-PR*, Rand Corp., Santa Monica, CA, 1967.
2. P. M. Lloyd and P. K. Stansby, 'Shallow-water flow around conical islands of small side slope', *ASCE J. Hydraul. Eng.*, in press.
3. M. Kawahara, M. Kobayashi and K. Nakata, 'Multiple level finite element analysis and its application to tidal current flow in Tokyo Bay', *Appl. Math. Model.*, **7**, 197–211 (1983).
4. D. R. Lynch and F. E. Werner, 'Three-dimensional hydrodynamics on finite elements. Part II: Nonlinear time-stepping', *Int. j. numer. methods fluids*, **12**, 507–533 (1991).
5. B. L. Lin and R. A. Falconer, 'Tidal flow and water quality modelling using the ULTIMATE QUICKEST scheme', *ASCE J. Hydraul. Eng.*, in press.
6. V. Casulli and R. T. Cheng, 'Semi-implicit finite-difference methods for three-dimensional shallow-water flow', *Int. j. numer. methods fluids*, **15**, 629–648 (1992).
7. N. A. Phillips, 'A coordinate system having some special advantages for numerical forecasting', *J. Meteorol.*, **14**, 184–185 (1957).
8. R. E. Uittenbogaard, J. A. Th. M. van Kester and G. S. Stelling, 'Implementation of three turbulence models in 3D-TRISULA for rectangular grids', *Rep. Z81/Z162*, Delft Hydraulics, 1992.
9. P. K. Stansby and P. M. Lloyd, 'A semi-implicit Lagrangian scheme for 3-D shallow-water flow with a two-layer turbulence model', *Int. j. numer. methods fluids*, **20**, 115–133 (1995).
10. A. M. Davies and J. E. Jones, 'On the numerical solution of the turbulence energy equations for wave and tidal flows', *Int. j. numer. methods fluids*, **12**, 17–41 (1991).
11. C. G. Speziale, 'On nonlinear k–l and k–ε models of turbulence', *J. Fluid Mech.*, **178**, 459–475 (1987).
12. P. Justesen, 'Prediction of turbulent oscillatory flow over rough beds', *Coastal Eng.*, **12**, 257–284 (1988).
13. W. Rodi, *Turbulence Models and Their Applications in Hydraulics*, 2nd edn, IAHR, Delft. 1984.
14. G. S. Stelling and J. A. Th. M. van Kester, 'On the approximation of horizontal gradients in σ coordinates for bathymetries with steep bottom slopes', *Int. j. numer. methods fluids*, **18**, 915–936 (1994).
15. H. Baumert and G. Radach, 'Hysteresis of turbulent kinetic energy in nonrotational tidal flows: a model study', *J. Geophys. Res.*, **97**, 3669–3677 (1992).
16. R. L. Haney, 'On the pressure gradient force over steep topography in σ coordinate ocean models', *J. Phys. Oceanogr.*, **21**, 610–619 (1991).
17. B. Van Leer, 'Upwind difference methods for aerodynamic problems governed by the Euler equations', *Lect. Appl. Math.*, **22**, 327–336 (1995).
18. P. K. Sweby, 'High resolution schemes using flux limiters for hyperbolic conservation laws', *SIAM J. Numer. Anal.*, 995–1011 (1984).
19. B. Koren, 'A robust upwind discretization method for advection, diffusion and source terms', in C. B. Vreugdenhil and B. Koren (eds), *Notes on Numerical Fluid Mechanics*, Vol. 4, *Numerical Methods for Advection–Diffusion Problems*, 1993, pp. 117–138.

